The effect of coupled friction and adhesion on the rheology of non-Brownian dense suspensions

The effect of coupled friction and adhesion on the rheology of non-Brownian dense suspensions

Michel Orsi, Laurent Lobry, Elisabeth Lemaire, and François Peters
Université Côte d'Azur, CNRS, Institut de Physique de Nice (INPHYNI), France

(*Electronic mail: michel.orsi@polito.it)

(Dated: 3 May 2025)

The role of adhesion between particles on the rheology of non-Brownian frictional suspensions undergoing simple shear flow is investigated numerically. To this purpose, we use two different numerical methods, namely the force coupling method (FCM) and the fictitious domain method (FDM). Intensity of adhesion, volume fraction, and friction coefficient are separately varied. The parameter space to be explored is first constrained by analyzing particle depletion and shear banding phenomena near the bounding walls under conditions of low volume fraction and applied stress. It is then shown that the relative viscosity of the suspension is a function of both volume fraction ϕ and shear stress Σ_{12}. The variation of the viscosity with these two parameters may be understood in the usual frame of suspension jamming, provided that the friction-dependent maximum volume fraction, ϕ_{m}^{μ} now depends on the dimensionless suspension stress $\sigma^* = 6\pi\Sigma_{12}a_1^2/F^{adh}$ that involves the adhesive force between particles F^{adh}, and the particle radius a_1. The variation of the maximum volume fraction with stress may be interpreted as the variation of the yield stress with volume fraction. This curve separates the plane (ϕ, σ^*) into two regions: one in which the suspension flows and the other in which it does not. The contribution of contact forces to normal stresses is also investigated. Its behavior differs markedly from that of non-adhesive particle suspensions, especially at moderate volume fraction.

I. INTRODUCTION

The influence of attractive forces on the structure and rheology of colloidal suspensions has been extensively studied, at least in the Brownian regime (see Larson [1], Mewis and Wagner [2] for reviews). Even at low volume fraction, such suspensions may form a gel with finite elasticity and yield stress and present shear-thinning behavior connected with apparent yield stress at high shear stress. More generally, Brownian suspensions display a large variety of complex mechanical behaviors, from soft gel to Newtonian liquid, closely connected to their microstructure (see Koumakis *et al.* [3] and references therein).

Non-Brownian (NB) suspensions also display a rich variety of behaviors, including shear-thickening[4], shear-thinning[5,6] and yield stress[7–9]. The nature of particle interactions, predominantly contacts, has been found to play a primary role in these behaviors[10]. For instance, friction has been shown to enhance shear viscosity[11,12], providing an explanation for the long-standing issue of discontinuous shear-thickening[11,13,14] as a stress-induced lubricated-to-frictional transition[15]. Load-dependent friction may induce shear-thinning, as shown in simulations[6] and confirmed in AFM measurements in colloidal probe mode[16,17]. In both cases, the transition reflects the variation of the maximum volume fraction with stress.

Attractive forces also have strong effects on the coupled microstructure and rheology of NB suspensions, depending on the volume fraction, and may originate from van der Waals forces[2], polymer depletion interactions[3], polymer chains entanglement[18] or capillary bridges[19]. They may be measured in situ using AFM colloidal probe techniques[20,21]. In sheared suspensions at low concentration, adhesion causes floc formation, or dynamic clusters that are largely independent of one another: the flow both influences and is affected by the instantaneous structure of the flocs. The flow pulls particles apart, potentially shattering the aggregates, and it also speeds up the rate of aggregation by bringing them together more quickly. The shear rate determines the size of these clusters; the larger the shear rate, the smaller the flocs, as shown in two-dimensional simulations[22] and in experiments[23]. The shear viscosity of such dilute suspensions under high stress is enhanced by adhesion, and significant shear-thinning is evidenced[22,23]. NB suspensions of adhesive particles display yield stress behavior both at high concentration[7,8] and at volume fraction as low as 2-3 %[24]. At such low concentration, the variation of the viscosity with shear rate is correlated with the size of the clusters, which increases as the shear rate decreases[24]. At a higher volume fraction, $\phi = 0.44$, experiments devoted to the rheology of weakly Brownian suspensions[3] showed a transition from yielding to Newtonian behavior around a quite high Péclet number (~ 100), suggesting a limited impact of Brownian motion on the transition. The latter turned out to be correlated with a microstructural transition from large heterogeneous structures at low stress to a more homogeneous solid distribution at high stress. The authors also performed Brownian dynamics numerical simulations of adhesive frictionless suspensions. They defined a modified Péclet number, Pe_{dep}, which measures the ratio of the shear to attractive forces, and they showed that the mentioned transition occurs at $Pe_{dep} \sim 1$.

Regarding the suspension modeling, Zhou, Uhlherr, and Luo [7] performed extensive shear viscosity measurement in suspensions of different micron-sized particles in an aqueous solution of glycerine and in water at different pH conditions, varying volume fraction and stress. They rationalized the experimental data by analogy with suspensions of non-adhesive particles, using the usual maximum volume fraction, which in the case of adhesive particles is shown to depend on the applied shear stress, i.e., on the ratio of the stress to a typical stress that reflects the attractive particle interactions. This stress-dependent maximum volume fraction is shown to ac-

count for the volume fraction-dependent yield stress. Later, this idea was highlighted by Barnes [25]. More recently, the main theoretical model that accounts for the stress-induced shear-thickening transition[26] has been generalized to tackle other constraints applied to the contacting particles motion in addition to sliding friction, such as adhesion or rolling friction[27], which may affect the maximum volume fraction, resulting in non-Newtonian behavior. This model successfully explained the variation of the shear viscosity of suspensions of adhesive spherical particles with volume fraction and stress, as measured in experiments[8]. In more detail, the experiments evidenced yield stress and shear-thinning, which could be understood as the result of a stress-dependent maximum volume fraction, involving a typical adhesion stress Σ_{adh} that is related to the force necessary to break the adhesive bonds between the particles. At high stress, where adhesive forces are completely overcome by hydrodynamic and compressive contact forces, the maximum volume fraction takes the usual non-adhesive frictional value ϕ_μ, while at low stress, the adhesive forces are predominant, resulting in the adhesion loose packing volume fraction ϕ_{alp}. From the experimental data, ϕ_{alp} was estimated around 0.35, but values as low as 0.18 were estimated in suspensions of calcite particles[28]. A recent experimental study[9] evidenced the shear-thinning of soft adhesive particles suspensions. The variation of the maximum volume fraction with stress was shown to exhibit the same type of transition from low value at low stress to higher value at high stress, in agreement with the mentioned modeling[8,27]. In particular, the limiting values of the maximum volume fraction at high stress were found consistent with computations from simulations of non-adhesive frictional particles. In addition, in the low stress regime, ϕ_{alp} was shown to decrease significantly as particle rigidity was decreased. Finally, it should be noted that adhesive forces have also been found to alter the shear-thickening transition in experiments[28,29].

Simulations of the slow flow of non-Brownian suspensions of attractive and frictional particles are scarce in the literature. Using a discrete element method to study the shear-thickening transition at high volume fraction, Pednekar, Chun, and Morris [30] showed that strong enough attractive (van der Waals) forces may overcome repulsion at low stress, and thus obscure the shear-thickening transition, in agreement with experimental works[28,31,32]. In a later study, Singh *et al.* [33] showed that, at the high volume fraction of interest and for high enough attractive forces, suspension flow is possible only in a bounded range of stress, smaller than the onset stress for shear-jamming and higher than the yield stress. In addition, the yield stress they measured is consistent with the modeling by Zhou, Uhlherr, and Luo [7] of a stress-dependent maximum volume fraction (supplementary material of Ref.[33]). It should be noted that simulations of dry granular packing evidenced a strong influence of short range attractive forces[34] or adhesive contact forces[35] on the resulting packing fraction, allowing the latter to decrease to approximately 0.14 at high adhesion and friction coefficient[35]. In the weakly-Brownian regime, the simulations by Koumakis *et al.* [3] of attractive frictionless suspensions at the single volume fraction $\phi = 0.44$ evidenced the stress-induced transition at high Péclet number from yield stress to Newtonian behavior, highlighting the ratio of the stress to a typical adhesion stress, $Pe_{dep} = \Sigma/\Sigma_{adh}$, as the control parameter. Finally, we note that attractive forces were shown to result in specific non-Newtonian behavior in oscillatory shear, promoting irreversibility at low stress accompanied by particle clustering[36].

In the present article, we aim at uncovering the coupled influence of friction and adhesion on the rheology of NB suspensions. To this purpose, we use particle resolved numerical simulations using two different methods, namely the Fictitious Domain Method[37] and the Force Coupling Method[38], which both account for hydrodynamic interactions and frictional adhesive contact forces. In more detail, we try to provide a consistent picture of the influence on the rheology of the volume fraction ϕ, microscopic friction coefficient μ_s, and particle adhesion force F^{adh}. The computations are rationalized in a frame close to the modeling by Zhou, Uhlherr, and Luo [7] and Richards *et al.* [8], i.e., using a friction- and stress-dependent maximum volume fraction ϕ_m^μ. Besides the friction coefficient, the relevant parameter here is, as mentioned above, the ratio of shear forces to adhesive forces $6\pi a^2\Sigma_{12}/F^{adh}$, which involves the shear stress Σ_{12}, particle radius a, and adhesive force F^{adh}.

The first section is devoted to the numerical model that we use, including the adhesive contact model, and to the presentation of the numerical set-up and the simulation parameters. We then turn to the numerical results. After a short comparison of the two methods for non-adhesive suspensions, the shear-banding observed at low stress is studied and the parameter range allowing for a proper computation of the rheological quantities (viscosity, shear rate, etc.) is determined. The next section is devoted to the influence of friction and adhesion on the constitutive laws. The stress-dependent maximum volume fraction is extracted from the viscosity measurements, seemingly unifying the description of adhesive and non-adhesive suspensions. Then, other quantities related to the normal stresses are examined, showing significantly different behaviors of adhesive and non-adhesive suspensions. A qualitative explanation is provided for these differences based on the contact force microstructure.

II. NUMERICAL METHODS

As introduced above, the simulations were conducted using two different methods, the Fictitious Domain Method (FDM) and the Force Coupling Method (FCM). These methods share some common features, but they also present differences, regarding both the applied boundary conditions and the way the control parameters are varied, as explained in the following.

A. The Fictitious Domain Method

1. General equations

The FDM has been detailed in the past[12], including the specific version that is used in the present article[37,39]. Its main

features are recalled here. In the FDM, the flow of a Newtonian liquid with dynamic viscosity η and density ρ is computed in the whole meshed simulation domain $\mathscr{D}$ including the particles. The latter are rigid spheres with the same density as the liquid. The rigidity of the particles is enforced using a force density $\rho\boldsymbol{\lambda}$ that acts only within the volume of each particle $\mathscr{D}_p$. In the present work, inertia is neglected for both the fluid and the particle dynamics. As a consequence, the fluid velocity $\mathbf{u}$ and pressure P obey modified Stokes equations:

$$\boldsymbol{\nabla}\cdot\boldsymbol{\sigma}+\rho\boldsymbol{\lambda}=\mathbf{0}\,,\quad \boldsymbol{\nabla}\cdot\mathbf{u}=0\,, \tag{1}$$

$$\boldsymbol{\sigma}=-P\boldsymbol{\delta}+\eta\left(\boldsymbol{\nabla}\mathbf{u}+\boldsymbol{\nabla}\mathbf{u}^{\mathrm{T}}\right)\,, \tag{2}$$

with the constraint that the fluid inside each particle (p) undergoes rigid body motion:

$$\mathbf{u}(\mathbf{x})=\mathbf{U}_p+\boldsymbol{\Omega}_p\times(\mathbf{x}-\mathbf{x}_p)\quad\text{for }\mathbf{x}\in\mathscr{D}_p\,, \tag{3}$$

where the particle translational and rotational velocities are respectively denoted by $\mathbf{U}_p$ and $\boldsymbol{\Omega}_p$.

Here, particles are subjected to hydrodynamic and contact forces only, and Newton's equations write for each particle:

$$\mathbf{F}_p^h+\mathbf{F}_p^c=\mathbf{0}\,,\quad \mathbf{T}_p^h+\mathbf{T}_p^c=\mathbf{0}\,, \tag{4}$$

where $\mathbf{F}_p^h$ and $\mathbf{F}_p^c$ respectively stand for the hydrodynamic and contact forces exerted on the particle (p), and $\mathbf{T}_p^h$ and $\mathbf{T}_p^c$ are the corresponding torques. The contact forces and torques will be detailed in the following.

The hydrodynamic forces and torques are split into two contributions. The first part corresponds to the force moments that originate in the fluid flow computed by the solver. The resulting forces and torques are hereafter denoted by $\mathbf{F}_p^{FDM}$ and $\mathbf{T}_p^{FDM}$. They are computed according to:

$$\mathbf{F}_p^{FDM}=-\rho\int_{\mathscr{D}_p}\boldsymbol{\lambda}\,\mathrm{d}\mathscr{V}\,,\quad \mathbf{T}_p^{FDM}=-\rho\int_{\mathscr{D}_p}(\mathbf{x}-\mathbf{x}_p)\times\boldsymbol{\lambda}\,\mathrm{d}\mathscr{V}\,. \tag{5}$$

However, the solver cannot properly compute the flow between particles when their surfaces are closer than the mesh grid size. As a consequence, the hydrodynamic stress moments applied to the particles, i.e. the hydrodynamic force, torque and stresslet (see Section II A 2 for the definition of the latter), must be corrected using theoretical expressions. The method that we follow for this purpose in the present article has been fully explained and validated by Orsi, Lobry, and Peters [37]. The generalized particle velocity and sub-grid (SG) force vectors are respectively denoted by $\boldsymbol{\mathcal{U}}=(\mathbf{U}_1,\,\mathbf{U}_2,\,\ldots,\,\boldsymbol{\Omega}_1,\,\boldsymbol{\Omega}_2,\,\ldots)$ and $\boldsymbol{\mathcal{F}}^{SG}=\left(\mathbf{F}_1^{SG},\,\mathbf{F}_2^{SG},\,\ldots,\,\mathbf{T}_1^{SG},\,\mathbf{T}_2^{SG},\,\ldots\right)$. The latter may be computed from the former using the sub-grid resistance matrix $\boldsymbol{\mathcal{R}}_{\mathscr{F}\mathscr{U}}^{SG}$:

$$\boldsymbol{\mathcal{F}}^{SG}=-\boldsymbol{\mathcal{R}}_{\mathscr{F}\mathscr{U}}^{SG}\cdot\boldsymbol{\mathcal{U}} \tag{6}$$

Here, the subscript $\mathscr{F}\mathscr{U}$ refers to the coupling between forces $(\mathscr{F})$ and velocities $(\mathscr{U})$, including both translational and rotational components. The SG resistance matrix depends on the fluid viscosity, particle positions, and radii, and is computed pairwise. The total hydrodynamic force and torque read:

$$\mathbf{F}_p^h=\mathbf{F}_p^{FDM}+\mathbf{F}_p^{SG}\,,\quad \mathbf{T}_p^h=\mathbf{T}_p^{FDM}+\mathbf{T}_p^{SG}\,. \tag{7}$$

Eq. (6) deserves several comments. First, unlike the standard sub-grid corrections, no mention of the ambient velocity field is made, meaning that only the particle velocities are needed to compute the sub-grid forces. Such an expression has been fully justified by Orsi, Lobry, and Peters [37] and stems from the fact that only lubrication flows that involve the relative velocities of particle surfaces are missed by the fluid solver, and consequently have to be considered for the corrections. It should also be noted that the same type of corrections has to be applied for particles close to bounding walls when particle-wall interactions have to be considered[37].

Eqs. (1)–(6) must be solved at each time step. The unknown quantities are the pressure and velocity fields $(P,\mathbf{u})$, the force density $\rho\boldsymbol{\lambda}$, and the particle velocities $\mathbf{U}_p$ and $\boldsymbol{\Omega}_p$. The main issue lies in the determination of the force density that allows proper accounting for the constraints imposed on the particles, namely particle rigidity – Eq. (3) – and particle momentum balance – Eq. (4). The numerical method followed to solve this problem has been explained in detail by Orsi, Lobry, and Peters [37]. In particular, to solve the involved equations efficiently, the method has been implemented within the OpenFOAM toolbox, which supports parallel computing.

2. Suspension rheology

Hydrodynamic contribution

Computing the effective stress in a suspension of solid particles requires the first moment of the hydrodynamic surface stress acting on each particle[40–42]:

$$\begin{aligned}\mathbf{D}_p^{FDM}&=\int_{\partial\mathscr{D}_p}(\boldsymbol{\sigma}\cdot\mathbf{n})\otimes(\mathbf{x}-\mathbf{x}_p)\;\mathrm{d}\mathscr{S}\\&=-\rho\int_{\mathscr{D}_p}\boldsymbol{\lambda}\otimes(\mathbf{x}-\mathbf{x}_p)\;\mathrm{d}\mathscr{V}-\left(\int_{\mathscr{D}_p}P\,\mathrm{d}\mathscr{V}\right)\boldsymbol{\delta}\,.\end{aligned} \tag{8}$$

where the second equality is obtained using Eqs. (1) and (2)[37]. The symbol $\otimes$ represents the outer product of vectors, with components given by $(\boldsymbol{A}\otimes\boldsymbol{B})_{ij}=A_iB_j$.

The antisymmetric part of the force dipole $\mathbf{D}_p^{FDM}$ is a tensor whose components are the components of the hydrodynamic torque $\mathbf{T}_p^{FDM}$ exerted on particle (p), while the symmetric part is usually called stresslet. The latter is split into the deviatoric part $\mathbf{S}_p^{FDM}$ and the isotropic part $s_p^{FDM}/3\,\boldsymbol{\delta}$, where s_p^{FDM} stands for the trace of the force dipole[43]. As a consequence, the FDM traceless stresslet, stresslet trace, and force dipole write:

$$\begin{aligned}\mathbf{S}_p^{FDM}&=-\rho\int_{\mathscr{D}_p}\left\{\frac{1}{2}\left[\boldsymbol{\lambda}\otimes(\mathbf{x}-\mathbf{x}_p)+(\mathbf{x}-\mathbf{x}_p)\otimes\boldsymbol{\lambda}\right]+\right.\\&\qquad\left.-\frac{1}{3}\boldsymbol{\lambda}\cdot(\mathbf{x}-\mathbf{x}_p)\,\boldsymbol{\delta}\right\}\mathrm{d}\mathscr{V}\,,\\ s_p^{FDM}&=-\int_{\mathscr{D}_p}\left[\rho\boldsymbol{\lambda}\cdot(\mathbf{x}-\mathbf{x}_p)+3P\right]\mathrm{d}\mathscr{V}\,,\\ \mathbf{D}_p^{FDM}&=\mathbf{S}_p^{FDM}+\frac{s_p^{FDM}}{3}\boldsymbol{\delta}-\frac{1}{2}\boldsymbol{\varepsilon}\cdot\mathbf{T}_p^{FDM}\,.\end{aligned} \tag{9}$$

where ε stands for the Levi-Civita symbol. We note that a reference has to be defined for the pressure. It has been chosen as the mean pressure over the whole simulation volume, meaning that $\int_D P \, \mathrm{d}\mathscr{V} = 0$ at each time step.

As in the case of the force and torque, an SG correction must be added to the FDM stresslet on the particles, which is computed using specific resistance SG matrices[37]. The total hydrodynamic traceless stresslet, stresslet trace, and force dipole are then computed as:

$$\mathbf{S}_p^h = \mathbf{S}_p^{FDM} + \mathbf{S}_p^{SG} \,, \quad s_p^h = s_p^{FDM} + s_p^{SG} \,, \quad \mathbf{D}_p^h = \mathbf{D}_p^{FDM} + \mathbf{D}_p^{SG} \,. \tag{10}$$

Contact contribution

The contact model employed in the present work will be detailed in Section II D. When contact occurs, it results in a force exerted by particle (q) on particle (p), $\mathbf{F}_{pq}^c$. The corresponding contact torques on particles (p) and (q) are computed from the tangential component of the force as:

$$\mathbf{T}_{pq}^c = \frac{a_p}{a_p + a_q} \mathbf{x}_{pq} \times \mathbf{F}_{pq}^{c,t} \tag{11}$$

where a_p and a_q stand for the particle radii, and $\mathbf{x}_{pq} = \mathbf{x}_q - \mathbf{x}_p$ is the distance between the particle centers. Contact forces also induce an additional stresslet which is given to the contacting particles (p) and (q) by:

$$\mathbf{S}_{pq}^c = \frac{1}{2} \frac{a_p}{a_p + a_q} \left(\mathbf{F}_{pq}^c \otimes \mathbf{x}_{pq} + \mathbf{x}_{pq} \otimes \mathbf{F}_{pq}^c \right) \tag{12}$$

The induced contact force dipole is written as follows:

$$\mathbf{D}_{pq}^c = \mathbf{S}_{pq}^c - \frac{1}{2} \boldsymbol{\varepsilon} \cdot \mathbf{T}_{pq}^c \tag{13}$$

The stresslet in Eq. (12) is not traceless, and its trace determines the contribution of contact forces to particle pressure. Finally, the same contact model is used for particle-wall interactions, and contributes to the particle force dipole.

B. The Force Coupling Method

The FCM is a particle-resolved simulation method of non-Brownian suspensions, and has been presented[44] and extensively validated in the past[38,44], including the present implementation[6,45]. A short, insightful presentation may also be found in the review by Maxey[46]. Only the main features are recalled here. As in the FDM, the Stokes flow of a Newtonian liquid is computed all over the meshed domain. Each particle is made globally rigid (zero mean deformation) using a force density as in Eq. (1), which also reflects the particle momentum and angular momentum balance. For each particle, this force density is made of a force monopole and a force dipole, both regularized, i.e., with a spatial extension, which account for the force, torque and stresslet exerted by the particle on the fluid. It is determined at each time step, as in the FDM. The hydrodynamic forces, torques and stresslets from the force density are supplemented by corrections to account for the unresolved SG flow between particles, in a way similar to the FDM. The FCM particle stresslet is extracted from the force density, and SG corrections are added too.

One important difference with the FDM in the present simulation is the set of boundary conditions. While the FDM box is sheared by rigid walls, the FCM as implemented here uses Lees-Edwards periodic conditions to generate the shearing motion, allowing in particular the use of a spectral solution method based on Fast Fourier Transform[47]. As a consequence, the FDM simulations provide information about the influence of the bounding walls on the rheology, which is of interest from an experimental perspective. However, as shown in the following, both methods give similar results in the central region outside the immediate vicinity of the walls.

C. Notes on the choice of the numerical methods

Both methods share strong similarities. In each case, the fluid flow is computed over the meshed domain, which ensures accurate treatment of long-range hydrodynamic interactions, albeit at a significantly higher computational cost compared to particle-based methods like the Discrete Element Methods[11,48]. This approach remains particularly relevant at moderate volume fractions. Moreover, sub-grid corrections are essential to capture lubrication forces, which dominate hydrodynamic interactions in the high volume fraction regime.

The main difference, from the perspective of the present study, lies in the way the shear flow is imposed through the boundary conditions. The FCM, as thoroughly described by Yeo and Maxey [38], employs Fast Fourier Transform to solve the Stokes Equations, enabling efficient computation in a volume that is periodic in all three directions. As mentioned earlier, shear flow is applied using Lees-Edwards boundary conditions, thus avoiding the use of physical shearing walls. Our implementation is designed for shared-memory architectures, allowing the flow computation to utilize all cores of a single processor. In contrast, the FDM is implemented within the OpenFOAM toolbox, leveraging its parallelization capabilities based on the MPI standard, which enables computations across multiple multi-core processors. While flow computation in OpenFOAM is already parallelized, we also parallelized the resolution of the particle sub-problem using the PETSc suite, which also relies on MPI. Various types of boundary conditions may be applied in OpenFOAM, but the most straightforward way to impose a shear flow is through the use of shearing walls, as described below.

Another key difference lies in the way the presence of the particles is accounted for. In the FDM, the force density within the particles is determined independently in every mesh cell. Local rigidity of the particle is enforced, which requires a relatively fine spatial resolution—namely, a mesh cell size equal to one fifth of the particle radius (Section II E)—and results in a large number of degrees of freedom per particle, corresponding to the force components applied on each internal mesh cell. As a result, sub-grid corrections are only applied

when particle surfaces are in close proximity, within the lubrication regime. These corrections depend solely on the relative particle velocities and not on the ambient shear flow[37], which is particularly relevant in nonhomogeneous flows[49], though perhaps less critical in the present context. In contrast, the FCM models particles via low-order stress moments, requiring only 11 degrees of freedom per particle. The force density is distributed over a volume larger than the physical particle, and rigidity is enforced globally rather than locally. This allows for a coarser mesh resolution—specifically, a mesh size of half the particle radius—compared to the FDM. Consequently, the FDM is expected to offer higher hydrodynamic accuracy, while the FCM is computationally more efficient due to the use of FFT-based solvers, lower spatial resolution, and a smaller number of degrees of freedom per particle. Nevertheless, a quantitative comparison of computational performance between the two methods is not provided, as our implementations rely on different parallelization strategies, and we performed a detailed scalability study only for the FDM[39].

Finally, despite the methodological differences, the close agreement between the results obtained with both approaches – as demonstrated in Howard, Maxey, and Gallier[50] and further illustrated below – strongly supports the reliability of our computations.

D. Contact model

Contact mechanics between two bodies is a complex domain, and real surface modeling involves many parameters, related to both the surface properties and the way they are loaded. For instance, large rough macroscopic bodies are known to experience contact through numerous asperities, which undergo elastic (and possibly plastic) deformation. The real contact area, which is very small compared to the apparent contact area, is then proportional to the load, resulting in the standard Amontons-Coulomb law of friction[51]. However, in the field of suspension rheology, it was recently shown that the long-standing issue of moderate shear-thinning behavior observed in non-Brownian suspensions could be explained in the frame of a mono-asperity contact model, where a single asperity is elastically deformed against another particle at low load, which results in a non-linear friction law[6,16]: the friction coefficient decreases as the load increases, thus resulting in shear-thinning. Adhesion adds some more complexity. Deformation occurs at zero load, meaning that a finite contact area develops in that case, so that a finite friction force should be overcome for sliding to occur. In addition, separating contacting bodies requires applying a finite traction. It has also been shown that, as expected, surface roughness may affect the adhesive forces[52,53].

The present study aims at exploring the basic influence of surface adhesion on the non-Brownian suspension rheology. To this purpose, a simple adhesive contact model was chosen, which only retains a minimal number of features. It is actually a simplified version of the more complete JKR model, well suited to the adhesive contact between smooth spheres[54] (see discussion in Appendix B). The normal force $\mathbf{F}_{pq}^{c,n} = -F_n \mathbf{x}_{pq}/\|\mathbf{x}_{pq}\|$ is the sum of a repulsive elastic force, obeying the classic Hertz law[51], and a constant attractive force F^{adh}, as represented in Fig. 1 [top,left]:

$$F_n = k_n \delta^{3/2} - F^{adh} \ . \tag{14}$$

This very basic contact model involves the roughness height h_r: contact occurs when the distance between the particles surfaces is smaller than h_r, i.e., when the compression δ is positive. The normal contact force is equal to the (negative) adhesive force when $\delta = 0$ (▲ in Fig. 1), and it is zero at a positive compression δ_0, where the compressive force balances the attractive force (● in Fig. 1). Thus, the normal force is attractive for $\delta < \delta_0$ and repulsive otherwise.

An elastic tangential force develops too, which is proportional to the sliding displacement (stick phase of the motion) $\mathscr{Y}$ between particle surfaces (more details in Peters *et al.*[45], Gallier *et al.*[55]):

$$\mathbf{F}_t = -k_t \mathscr{Y} \ . \tag{15}$$

The tangential force may increase up to a critical friction force, which triggers the slip phase of the motion. Then, $\mathbf{F}_t$ keeps constant in intensity and tangent to the particle surface. The critical force is assumed to be related to the contact area, i.e., to the normal elastic contribution, as follows:

$$F_t = \mu_s \left(F_n + F^{adh} \right) \ . \tag{16}$$

Eqs. (14) and (16) deserve a few comments. As already mentioned, the model retains important features: at zero load, finite deformation – $(F^{adh}/k_n)^{2/3}$ – as well as finite resistance to sliding motion – $\mu_s F^{adh}$ – occur (● in Fig. 1). In addition, splitting apart two particles requires applying the traction F^{adh} (▲ in Fig. 1). It should also be noted that Eq. (16) is part of an early model of adhesive frictional contact[56]. However, as discussed in more detail in Appendix B, some features sound nonphysical, even in the simple case of the adhesive contact between smooth spheres. In particular, we note that the vanishing of the tangential force at $\delta = 0$ seems unrealistic, since the actual contact area is not expected to vanish at this point. In addition, contact hysteresis is not accounted for, meaning that, in the frame of the model, an existing contact cannot bear negative compression δ. Finally, even in the simplified case of the contact between two smooth spheres as described by Eq. (14), a non-linear relation between the contact area and the normal "elastic" force is expected (Appendix B), leading to a non-affine relation between F_t and F_n contrasting with Eq. (16). However, it should be noted that Eq. (16) has been evidenced in recent experimental friction coefficient measurement between colloidal particles using AFM techniques[29].

As a consequence, some model parameters may not bear strong physical meaning. In particular, when smooth spheres are considered, the stiffnesses, k_n and k_t, depend on the mechanical properties of the constituting material and the sphere radii[45,54]. In the present case, they are to be understood as a numerical tool allowing to generate contact forces.

In the same line, roughness is known to promote direct contact between particles[57,58], but the influence of the specific asperity size on the rheology of non-adhesive frictional

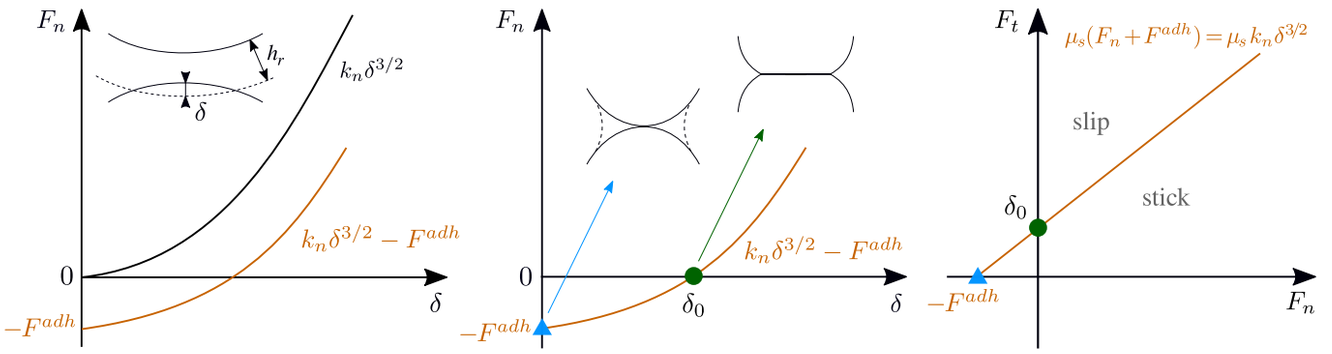

FIG. 1. Contact model: [top] normal force, and [bottom] threshold of the tangential force. $F_n = 0$ is reached at a positive compression δ_0, and a tangential force is still present (●). At $\delta = 0$ (▲), the tangential force vanishes and the normal one is the (negative) adhesive force.

particles in simulations is quite limited[55], at least when it is not coupled to a varying friction coefficient, for instance in a mono-asperity contact model[6,59]. We note here that the shear-thinning behavior observed in load-dependent friction coefficient is significantly weaker than in frictional adhesive particles suspensions (Section III), which justifies to tackle the latter independently, leaving aside the former in the present study. Nevertheless, h_r should be understood in the frame of the present model as the typical distance between particle surfaces below which contact forces outweigh the lubrication interactions. In particular, we do not intend to account for the influence of roughness on the adhesive forces[52,53].

Finally, in FDM simulations, the normal stiffness is selected to yield a typical particle compression $\bar{\delta}/h_r = \bar{\varepsilon} = 5 \cdot 10^{-2}$ in a sheared dilute suspension of non-adhesive particles[45]. Specifically, given that the typical hydrodynamic force between two particles, a_1 in radius, in a simple shear flow (in a dilute suspension) is $6\pi\eta a_1^2\dot{\gamma}_0$, the elastic parameter $\dot{\Gamma}$ as defined below is set to one:

$$\dot{\Gamma} = 6\pi\eta a_1^2\dot{\gamma}_0 / \left(k_n(\bar{\varepsilon}h_r)^{3/2}\right) = 1 \,. \tag{17}$$

In FCM simulations, $\dot{\Gamma}$ is varied depending on the adhesion strength, as detailed in Section II E 2, without significantly affecting the computed quantities.

The tangential stiffness obeys the expression[6,45,55,60]:

$$k_t = \frac{2}{7}k_n\sqrt{\delta} \,. \tag{18}$$

It is finally noted that particles are considered to be in contact when the gap between their hydrodynamic surfaces (i.e., the surfaces governing hydrodynamic lubrication) falls below h_r (Fig. 1), prior to any actual overlap. Nevertheless, high stress conditions may still lead to unwanted overlap. To prevent this, a supplementary repulsive force is activated as particles approach hydrodynamic contact.

E. Numerical setup

1. *Simulations with the FDM*

To avoid crystallization at high concentration, we consider bidisperse suspensions with particle radii a_1 and $a_2 = 1.4a_1$, with equal volume fractions. A domain with size $(L_x/a_1 \times L_y/a_1 \times L_z/a_1) = (20 \times 20 \times 20)$ is considered for all the FDM simulations. Various values of the mean volume fraction $\phi_0 \in [0.27, 0.58]$ are investigated, corresponding to a total number of particles N_p typically between 300 and 900. Three values of the friction coefficient are considered, namely $\mu_s \in \{0, 0.1, 0.5\}$, and the roughness height is chosen as $h_r/a_1 = 5 \cdot 10^{-3}$, which is consistent with experiments for model spherical polymer particles[61,62]. The velocity of the shearing walls is imposed, (Fig. 2 [left]) resulting in a constant apparent shear rate $\dot{\gamma}_0$.

Time, length, and forces are made dimensionless using respectively $1/\dot{\gamma}_0$, a_1, and $\eta\dot{\gamma}_0 a_1^2$, so that the remaining relevant dimensionless parameters in the simulations are:

- Elastic parameter $\dot{\Gamma} = 6\pi\eta a_1^2\dot{\gamma}_0/(k_n(\bar{\varepsilon}h_r)^{3/2})$, which is kept constant $\dot{\Gamma} = 1$ (Section II D).
- Adhesion parameter $G_0^{adh} = F^{adh}/(6\pi\eta a_1^2\dot{\gamma}_0) = \Sigma_{adh}/\eta\dot{\gamma}_0$, which reflects the competition between adhesion forces and hydrodynamic interactions in a dilute suspension. Σ_{adh} is

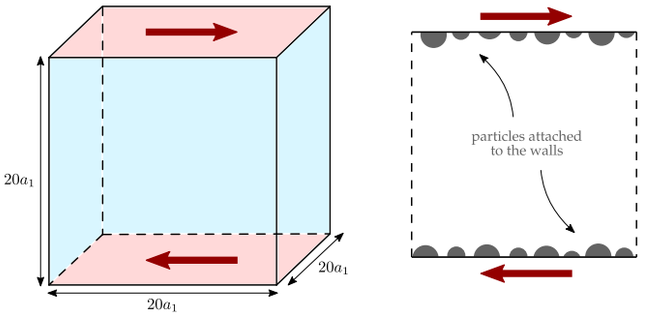

FIG. 2. [left] Numerical domain. [right] For $\mu_s = 0$ and $\mu_s = 0.1$, particles have been attached to the walls for more effective shearing.

the typical stress needed to separate two particles at contact. As G_0^{adh} involves the solvent viscosity only, and not the viscosity of the suspension $1/G_0^{adh}$ is actually to be considered a dimensionless shear rate in a concentrated suspension.

- Dimensionless time step $\dot{\gamma}_0 \Delta t$, which determines the stability of the particle motion. It is kept at the largest value that still allows smooth motion. This value is mostly connected with the evolution of the elastic tangential force Eq. (15), and has been set between $5 \cdot 10^{-6}$ and 10^{-4}, depending on the volume fraction and the adhesion parameter.

In experiments, the shear rate (or shear stress) is varied for given properties of the particles (stiffness, adhesive force, etc.). In that frame, both $\dot{\Gamma}$ and G_0^{adh} would vary, such that $\dot{\Gamma} \times G_0^{adh} = F^{adh}/(k_n(\bar{\varepsilon}h_r)^{3/2})$ is constant. This dimensionless number – $\dot{\Gamma} \times G_0^{adh}$ – determines the typical contact compression induced by the adhesive force. In contrast, in the FDM simulations, it is not kept constant, as $\dot{\Gamma}$ is fixed. The consequences of this choice are difficult to assess *a priori*. On the one hand, in suspensions of non-adhesive particles with a constant friction coefficient, variations of $\dot{\Gamma}$, which influence the typical contact compression due to hydrodynamic forces, have been shown to have a limited impact on the rheology of non-Brownian suspensions[55]. On the other hand, variations in compression lead to changes in adhesion energy, which could potentially impact the suspension rheology. Nevertheless, as discussed later, FCM simulations are conducted with constant $\dot{\Gamma} \times G_0^{adh}$, and they yield very similar results. This suggests that whether or not this product is kept constant has only a minor effect on the overall simulation results.

For each of the three values of the friction coefficient $\mu_s \in \{0, 0.1, 0.5\}$ considered here, sequences of equal or similar volume fractions ϕ_0 are chosen, for which the adhesion parameter G_0^{adh} is varied. In Table I, the parameters used in the simulations are gathered. The choice of the parameters deserves a few words. The main idea was to obtain data that fill a grid with more or less constant volume fractions and shear stresses. The simulations for $\mu_s = 0.5$ were first performed. In this case, the volume fraction ϕ_0 was kept constant for multiple values of G_0^{adh}. It was observed that, as explained in detail in the next sections, particle wall-depletion and shear-banding occurs, leading in particular to a value of the volume fraction in the core of the suspension (i.e., in the center of the system away from the walls) different from the mean volume fraction ϕ_0, with a significant influence of adhesion. In order to correct this behavior, for $\mu_s = 0$ and $\mu_s = 0.1$, a specific value of ϕ_0 was associated to each value of G_0^{adh}.

In addition, in an attempt to limit wall-depletion and shear-banding, for $\mu_s = 0$ and $\mu_s = 0.1$ particles have been "attached" to the walls (i.e., they have the same velocity as the walls), with the purpose to more efficiently shear the suspension using such a "bumpy" walls. To limit ordering of the attached particles and layering of the free particles at the boundaries, the particles are attached to the walls by considering a larger domain size in the direction of the walls when initially filling the domain with the specified volume fraction. For the cases presented here, the domain size is increased by a length equal to $1.4a_1$ for each wall during the filling.

Finally, the volume fractions probed for $\mu_s = 0$ and $\mu_s = 0.1$ have been chosen in general higher than for $\mu_s = 0.5$, because higher maximum volume fractions were expected.

TABLE I. Numerical parameters for the three values of the friction coefficient $\mu_s = [0,\ 0.1,\ 0.5]$: chosen volume fractions ϕ_0 and associated adhesive coefficients G_0^{adh} in FDM simulations.

$\mu_s = 0.5$	
ϕ_0 [%]	G_0^{adh}
27	97, 29, 14, 4.4, 2.66, 1.6, 0.66, 0.29
32	92, 37, 13.3, 7.3, 4.44, 2.3, 0.96, 0.37
37	104, 17.4, 9, 4.4, 1.67, 0.65
42	405, 53, 22.12, 11, 3.63, 1.2
45	377, 226, 44.72, 23, 6.54, 2.5
$\mu_s = 0.1$	
ϕ_0 [%]	G_0^{adh}
36, 36, 37, 37	9.34, 4.05, 1.9, 0.9
41, 41, 42, 42	17.9, 7.2, 3.27, 1.5
45, 45, 47, 47	30, 11.3, 6.92, 3
49, 50, 51, 52	84, 33, 17.1, 8.83
52, 54, 55, 56	336, 180, 93, 48
$\mu_s = 0$	
ϕ_0 [%]	G_0^{adh}
36, 36, 37, 37	4.71, 2.95, 1.72, 0.74
41, 41, 42, 42	13.5, 6.2, 2.85, 1.32
46, 46, 47, 47	24, 10.6, 5.46, 2.43
50, 51, 52, 53	54, 28, 14.4, 7.44
54, 56, 57, 58	216, 199, 103, 53

2. Simulations with the FCM

Simulations of bidisperse suspensions with the same size ratio as for the FDM ($a_2/a_1 = 1.4$) are performed over a cubic simulation domain, $(16a_1)^3$ in size. The domain is 3D-periodic, and Lees-Edwards periodic conditions are used to generate the shearing motion and the unit mesh cell size is set to $a_1/2$. The same dimensionless quantities are relevant as above. Three values of the mean volume fraction ($\phi_0 \in \{0.3, 0.4, 0.45\}$) and three values of the friction coefficient ($\mu_s \in \{0.3, 0.5, 1\}$) are considered. For each pair (ϕ_0, μ_s), values of the reduced adhesive force G_{adh} were evenly sampled between 0.2 and 10^3. The product $\dot{\Gamma} \times G_0^{adh} = F^{adh}/\left(k_n(\bar{\varepsilon}h_r)^{3/2}\right) = 0.9$, was kept constant for all simulations, consistently with what would happen in experiments when the shear rate is varied for a given suspension. This particular value implies that the typical asperity compression due to the adhesive force alone is $\bar{\delta}/h_r \sim 0.9\bar{\varepsilon} \sim 4.6 \cdot 10^{-2}$. As a consequence, the elastic parameter, $\dot{\Gamma}$, was varied approximately between 10^{-4} and 4.5. As already mentioned, this is in contrast with the FDM simulations, where $\dot{\Gamma}$ is kept equal to 1, with no significant discrepancy, though.

Due to the absence of rigid boundaries, the volume fraction is in general uniform, equal to ϕ_0. However, shear-banding may still occur at high adhesion, as noted below.

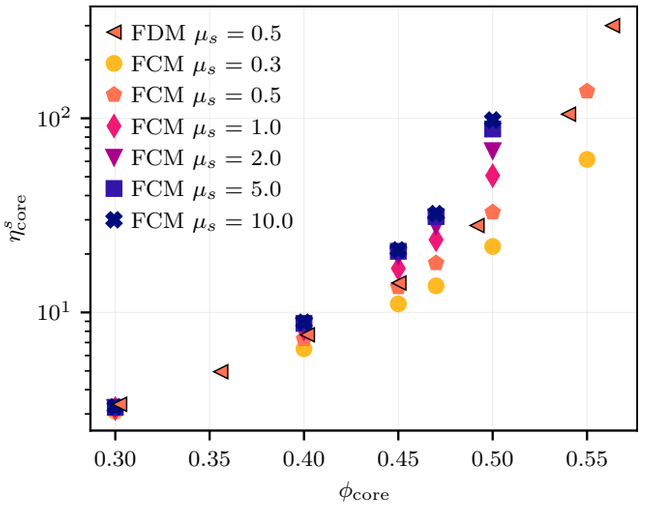

FIG. 3. Relative viscosity for non-adhesive frictional particle suspensions from FDM and FCM simulations. Each data set corresponds to a particular value of the friction coefficient μ_s.

III. RESULTS

A. Comparing FDM and FCM results for non-adhesive particle suspensions

Here, we show that FDM and FCM yield material functions in close agreement for nonadhesive suspensions, and recall some basic facts concerning frictional suspensions. We note that rheological quantities from FDM and FCM simulations of nonadhesive, frictionless particle suspensions have been shown to agree[50]. Here we consider the viscosity and reduced contact normal stresses in the shear plane, from both simulation methods, for nonadhesive suspensions, at $\mu_s = 0.5$.

Fig. 3 displays the relative shear viscosity from FDM ($\mu_s = 0.5$) and FCM simulations (data from Lobry *et al.*[6] for various friction coefficients). It is well known now that the shear viscosity of non-Brownian suspensions greatly increases with the friction coefficient[11,55], as also shown in Fig. 3, which is conveniently described by the variation of the maximum volume fraction with friction[6,63]. A clear agreement is observed between the data from both methods at $\mu_s = 0.5$.

Other quantities of interest are the reduced contact normal stresses $\hat{\Sigma}^c_{ii} = \Sigma^c_{ii}/\Sigma^s_{12}$, where $i \in \{1,2,3\}$ denote the directions of the velocity, the velocity gradient, and the vorticity in the simple shear flow. It should be noted that contact stresses drive shear-induced particle migration[41,42,64], and that the reduced contact stresses are directly involved in the migration in plane Poiseuille flow[49,65,66], in tube flow and in cylindrical Couette flow[67]. In Fig. 4, the normal contact stresses in the shear plane as a function of volume fraction are displayed. Again, a significant variation with the friction coefficient is observed in the FCM simulations, together with a close agreement between the FCM and FDM results for $\mu_s = 0.5$.

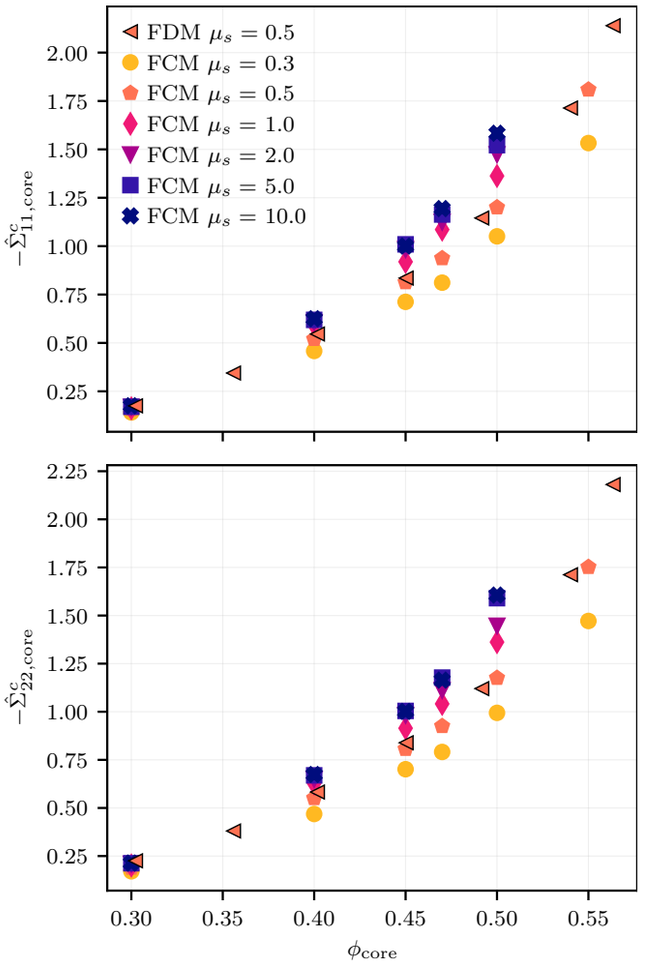

FIG. 4. Reduced contact normal stresses in the shear plane, $\hat{\Sigma}^c_{ii} = \Sigma^c_{ii}/\Sigma^s_{12}$, for non-adhesive frictional particle suspensions from FDM and FCM simulations. Each data set corresponds to a particular value of the friction coefficient μ_s.

B. Wall-depletion and shear-banding in bounded simulations

In FDM simulations, shearing motion is driven by rigid walls, which induce specific behaviors, namely wall-depletion and shear-banding. Such behaviors are of interest for at least two reasons: first, they have to be accounted for to extract reliable rheological quantities, and second, they are expected to take place in experiments, with the same consequences. In this way, simulations can be used to assess the experimental uncertainties or inaccuracies involved when the mean shear rate is used to calculate viscosity, and when the suspension is considered a homogeneous fluid.

1. Apparent and core quantities

The rigid driving walls are known to induce particle ordering close to them in monodisperse[12,44,66], or slightly bidisperse[37] suspensions. In the present case, particle de-

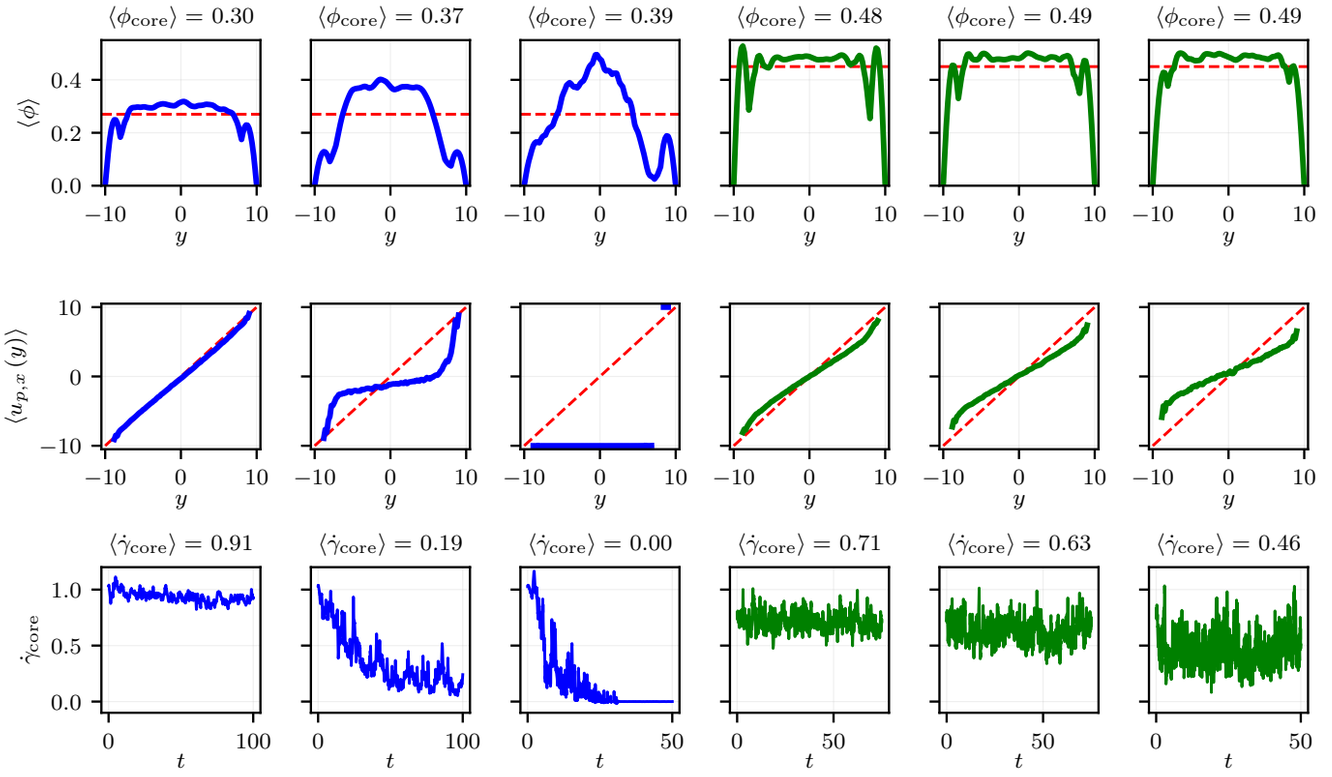

FIG. 5. Time-averaged volume fraction $\langle \phi(y) \rangle$ and particle velocity $\langle u_{p,x}(y) \rangle$ profiles, and evolution of the core shear rate $\dot{\gamma}_{\text{core}}$, for $\mu_s = 0.5$ and different adhesion parameters G_0^{adh} (increasing from left to right): (blue lines, upper three rows) results for $\phi_0 = 0.27$ ($G_0^{adh} = [0.29,\ 14,\ 97]$, $\sigma^* = [10.59,\ 0.4,\ 0.07]$), and (green lines, lower three rows) results for $\phi_0 = 0.45$ ($G_0^{adh} = [2.5,\ 23,\ 377]$, $\sigma^* = [7.84,\ 2,\ 0.82]$). Red dashed line: (top) mean volume fraction, (center) uniform shear rate velocity profile.

pletion at the walls is enhanced by adhesion, and results in enhanced wall-slip at high adhesion, which even turns into shear-banding at moderate volume fraction. Before these behaviors are addressed, various quantities are defined, which result from averaging either in the core homogeneous suspension (*core* quantities) or in the whole simulation domain (*apparent* quantities). In more detail, the apparent relative viscosity reads:

$$\frac{\Sigma_{12}}{\eta \dot{\gamma}_0} = \eta^s_{\text{app}} \,, \tag{19}$$

where Σ_{12} is the mean shear stress averaged over the whole simulation domain and over time in the stationary regime.

The *core* region is identified as the part of the domain in which both volume fraction and particle velocity profiles are homogeneous without any wall-induced structuration (typically, wall-layering occurs for $\approx 5a_1$ from each wall). In the suspension core, the shear rate $\dot{\gamma}_{\text{core}}$ is computed from the linear regression of the particle velocity profile and time-averaged over the steady regime. Since particle layering in the vicinity of the walls induces wall slip[49], the core shear rate is smaller than the apparent shear rate $\dot{\gamma}_0$ computed from the wall velocity, at least when the walls are not roughened using attached particles. In addition, the volume fraction in the wall area is smaller than in the core region, so that $\phi_{\text{core}} > \phi_0$. This leads to a measured core adhesive parameter G^{adh}_{core} and a core reduced shear stress:

$$\frac{F^{adh}}{6\pi\eta\dot{\gamma}_{\text{core}}a_1^2} = G^{adh}_{\text{core}} \,, \quad \frac{6\pi\Sigma_{12,\text{core}}a_1^2}{F^{adh}} = \sigma^* = \frac{\eta^s_{\text{core}}}{G^{adh}_{\text{core}}} \,, \tag{20}$$

where the core relative viscosity η^s_{core} is computed from the time-averaged core shear stress and shear rate as:

$$\frac{\Sigma_{12,\text{core}}}{\eta\dot{\gamma}_{\text{core}}} = \eta^s_{\text{core}} \,. \tag{21}$$

We recall that σ^* is the ratio of the shear stress to the typical stress needed to separate two particles at contact, $F^{adh}/\left(6\pi a_1^2\right)$.

2. *Wall-depletion and shear-banding*

In the cases of moderately concentrated suspensions and high adhesive forces, clear layers form in the vicinity of the rigid boundaries that result in wall-slip: this behavior is called hereafter *wall-depletion*. As adhesive forces are further increased, shear-banding occurs: the particles form a single cluster (sometimes two), stuck to one of the boundaries, which do not deform. In such cases, the core shear rate $\dot{\gamma}_{\text{core}}$ drops to very low values, sometimes exactly zero.

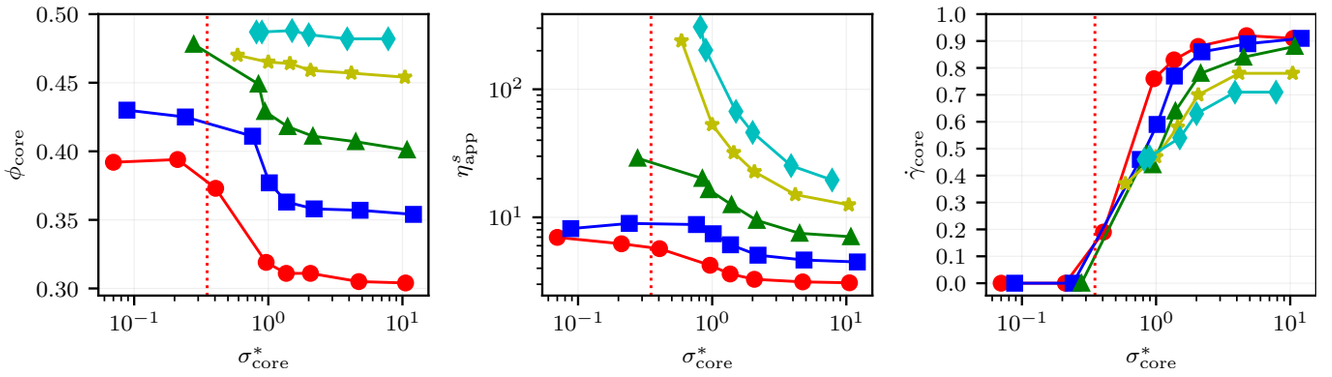

FIG. 6. Time-averaged (upper left) core volume fraction ϕ_{core}, (lower left) apparent relative viscosity η^s_{app}, and [right] core shear rate $\dot{\gamma}_{\text{core}}$, as a function of the reduced shear stress σ^*, for different values of ϕ_0 and with $\mu_s = 0.5$. Symbols: (●) $\phi_0 = 0.27$, (■) $\phi_0 = 0.32$, (▲) $\phi_0 = 0.37$, (★) $\phi_0 = 0.42$, (♦) $\phi_0 = 0.45$. The lines are a guide to the eye. Red dotted line: limit of the shear-banding regime.

To give a more precise picture of this behavior, an example is given in Fig. 5: the results for two mean volume fractions $\phi_0 = 0.27$ (blue lines, upper three rows) and $\phi_0 = 0.45$ (green lines, lower three rows), with same friction coefficient $\mu_s = 0.5$, and multiple adhesion parameters G_0^{adh} (increasing from left to right) are displayed. The steady volume fraction and particle velocity profiles, together with the temporal evolution of the core shear rate, are displayed. The spatial profiles are computed as in Orsi, Lobry, and Peters [37], Orsi *et al.* [49]. In the cases with low mean volume fraction and high adhesive forces (on the right of the upper three rows), particle clump together, leading to volume fraction profiles (time-averaged in the stationary regime) that are not constant in the core region, contrarily to the non-agglomerated cases with low adhesive forces (on the left of the upper three rows). Also, in the agglomerated cases the core shear rate decreases during the simulation run, and it can reach very low values, sometimes exactly zero, showing that the suspension is no longer deformed and agglomerates move as rigid bodies (Fig. 5).

The above-mentioned behavior is not observed in suspensions with high volume fractions, not even in the cases with the highest adhesive forces, as shown in the lower three rows of Fig. 5 (i.e., for $\phi_0 = 0.45$), where the suspension always shows a finite shear rate $\dot{\gamma}_{\text{core}}$ and the corresponding volume fraction profiles show a constant region in the core. It should also be noted that the rheological quantities may require a long time before reaching steady-state. It is therefore necessary to perform long simulations. Finally, all the simulations (showing a finite shear rate) have been run for a deformation of the core region during the steady regime of at least $\Delta\gamma_{\text{core}}^{steady} \sim 25$.

In the cases where $\dot{\gamma}_{\text{core}} \approx 0$, the core relative viscosity η^s_{core} cannot be defined. In Fig. 6 the results for $\mu_s = 0.5$ are shown, where the computed apparent relative viscosity is also displayed. In the agglomerated cases, η^s_{app} levels off due to shear-banding. We note that in the context of experimental measurements in the presence of shear-banding, a viscosity close to η^s_{app} is expected.

Fig. 6 displays the trends that have been explained above: at high mean volume fraction ϕ_0, reducing the stress induces a slight increase of the volume fraction, and a decrease of the core-shear rate, which keeps finite though. The viscosity seems to diverge, suggesting the existence of a yield stress. At a lower mean volume fraction, the viscosity increases too as the stress is decreased, but the conclusions are blurred by the concomitant increase of the core volume fraction. In that case, low-stress measurements are impeded due to shear-banding.

Finally, in both volume fraction ranges, homogeneous straining of the suspension is only possible for reduced stress larger than typically 1. This suggests that the yield stress satisfies the following intuitive relation:

$$\sigma_c^* \sim 1 \Leftrightarrow \Sigma_c \sim \frac{F^{adh}}{6\pi a_1^2}\,, \tag{22}$$

meaning that the stress needs to be high enough for the induced force between the particles to break adhesive bonds.

To conclude, it is quite difficult to simulate systems with $\sigma^* \lesssim 1$, with two different trends depending on the volume fraction ϕ_0: for $\phi_0 \gtrsim 0.4$, the core volume fraction slightly increases and the relative viscosity diverges as the stress decreases, clearly reflecting the yield stress. This requires decreasing the time step while approaching the yield stress, leading to an increasing computational cost. For $\phi_0 \lesssim 0.4$, the relative viscosity increases as the stress decreases, but now the core volume fraction strongly increases, leading to very low values of the core shear rate (often exactly zero) and results become unclear or unusable.

We recall that the case $\mu_s = 0.5$ has been addressed during the first simulations campaign, and, in some cases, shear-banding and wall-depletion were observed. For $\mu_s = 0$ and $\mu_s = 0.1$, we tried to avoid these behaviors: this is why, as previously mentioned, particles were attached to the walls (as shown in Fig. 2 [right]), in order to better shear the suspension. In Fig. 7, the volume fraction and particle velocity profiles as well as the temporal evolution of the shear rate are shown for $\mu_s = 0.1$, $\phi_0 = 0.36 - 0.37$, and different values of the adhesion parameter (increasing from left to right). We notice that the shear rate never reaches values close to zero (the results for $\mu_s = 0$, although not shown here, are analogous). Therefore, we have the feeling that the suspension is indeed better sheared in cases with high adhesion when particles are

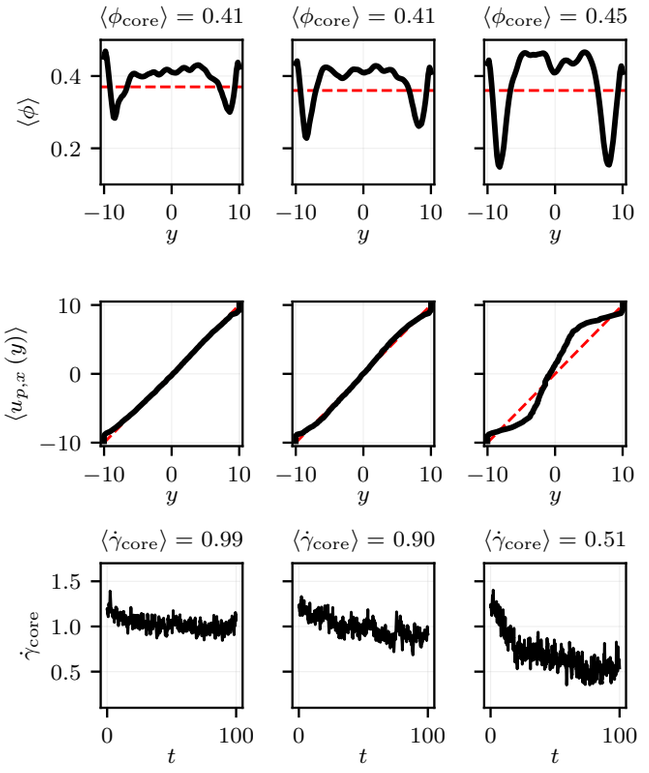

FIG. 7. Time-averaged (top) volume fraction $\langle \phi(y) \rangle$ and (center) particle velocity $\langle u_{p,x}(y) \rangle$ profiles, and (bottom row) evolution of the core shear rate $\dot{\gamma}_{\text{core}}$, for $\mu_s = 0.1$ and increasing adhesion parameter G_0^{adh} left to right: results for $\phi_0 = [0.37,\ 0.37,\ 0.36]$, $G_0^{adh} = [0.9,\ 1.9,\ 9.34]$, $\sigma^* = [7.71,\ 3.74,\ 0.98]$). Red dashed line: (top) mean volume fraction, (center) uniform shear rate velocity profile.

attached to the walls. However, a final conclusion about the effect of attaching particles to the walls cannot be drawn at this point, as a systematic comparison of simulations with smooth (but still frictional) and rough walls and with otherwise same parameters should be done. Also, we expect that roughening the walls is not completely sufficient to avoid shear-banding. Indeed, we tried to attach particles to the walls in one of the cases with $\mu_s = 0.5$ showing shear-banding, but the results showed no difference when compared with the ones obtained without using the roughened walls. Therefore, we expect this expedient to lower wall slip for quite concentrated suspensions only. Moreover, we note that the volume fraction at the walls is always larger than the mean volume fraction. This is related to how the system is initialized. As already mentioned, the particles are placed in a slightly larger box than the actual simulation domain, and the particles that undergo overlapping with the actual walls are frozen, forming the rough walls in the simulation. Since layering occurs during initialization, the volume fraction depends on the position relative to the walls, which is reflected in the final frozen particle distribution. Increasing the size of the box during preparation of the rough wall may improve this point.

The effect of the system size on shear-banding was not systematically performed, mostly due to the high computational cost. However, a system twice as large in the direction normal to the walls ($L_y/a_1 = 40$) was simulated, at a value of the parameters that displays shear-banding in the standard size ($\phi_0 = 0.27$, $G_0^{adh} = 97$). The latter behavior was still observed in the larger system. A more comprehensive study would be useful, but is out of the scope of the present article.

We note here that shear-banding is still observed in the FCM computation, where the shearing motion is not induced by rigid walls, but rather by periodic Lees-Edwards conditions. Even though lower stresses are reached ($\sigma^* \sim 0.7$), this suggests that rigid boundaries promote shear-banding, but that more fundamental mechanisms are also responsible for it.

C. Shear viscosity

1. *Bounded suspensions*

In this section, the rheological constitutive law for the shear stress is investigated, and the combined influence of both friction and adhesion is addressed. We focus here on the data from the FDM simulations, which is more complicated since neither the volume fraction nor the reduced stress are known in advance. From now on, all the quantities refer to the core homogeneous region, unless otherwise specified.

We previously explained that the relative viscosity η^s of a given suspension depends on two parameters: the volume fraction ϕ and the shear stress σ^*. However, only the apparent adhesion parameter G_0^{adh} is imposed in the present simulations, and not the reduced stress. In addition, the core volume fraction is not controlled either, but only measured. In order

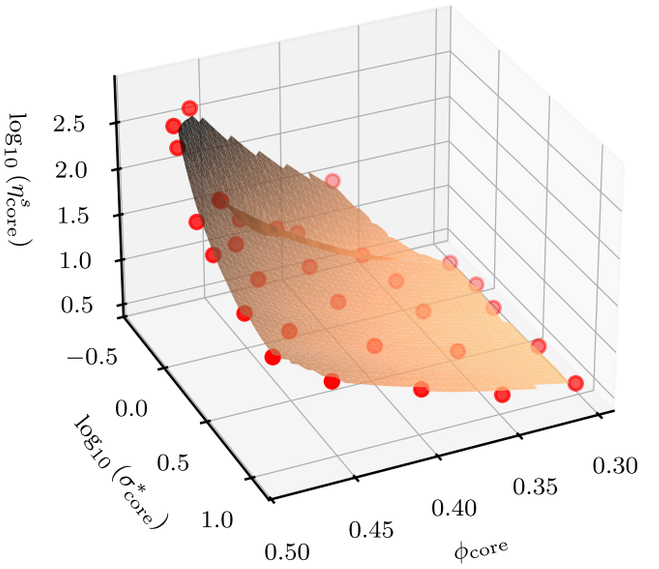

FIG. 8. Three-dimensional plot of the core relative viscosity η^s_{core} as a function of both the core volume fraction ϕ_{core} and the reduced shear stress σ^*, for $\mu_s = 0.5$. The raw data (•) have been interpolated along both ϕ_{core} and σ^*_{core} with a high number of interpolation points to obtain a smooth fine grid (surface).

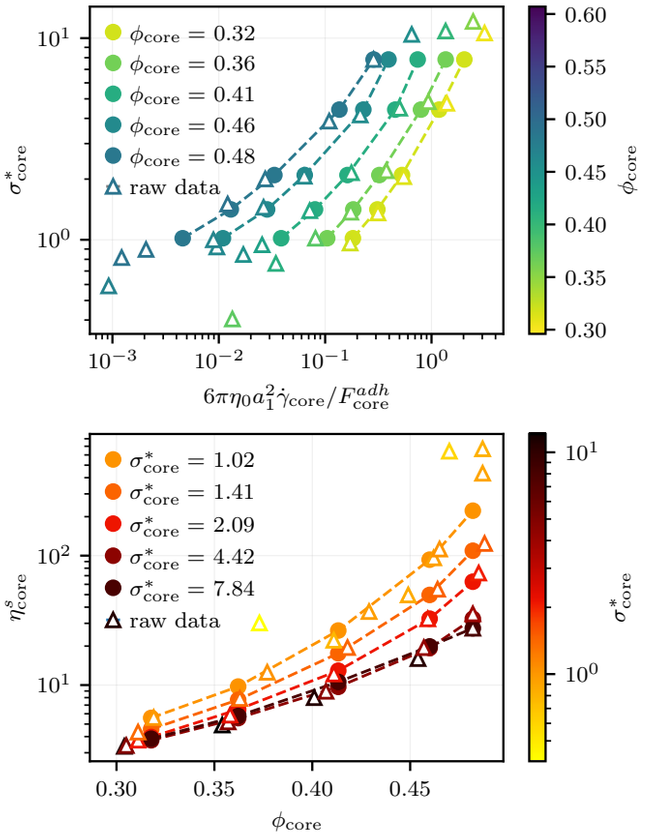

FIG. 9. The results for $\mu_s = 0.5$ are interpolated at selected values of core volume fraction and reduced shear stress.

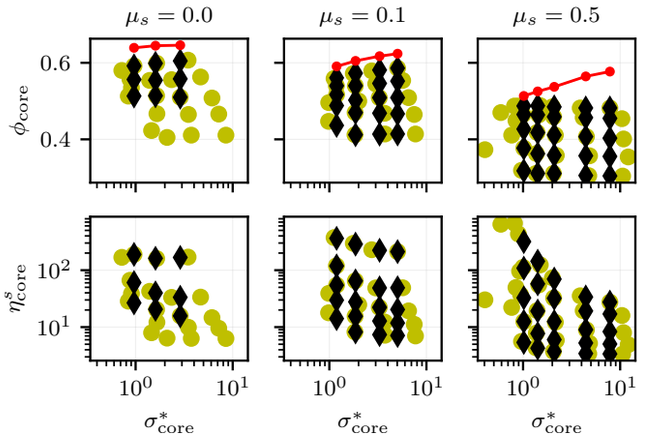

FIG. 10. (●) Core material functions for (left column) $\mu_s = 0$, (central column) $\mu_s = 0.1$, and (right column) $\mu_s = 0.5$: (top row) core volume fraction, (bottom row) core relative viscosity, as functions of the reduced shear stress. (◆) Data interpolated at constant shear stresses σ^*_{core}. (●) maximum volume fraction (Section III C 3)

to better understand the influence of adhesion on the relevant quantities, the data need to be interpolated. Here, only the interpolated data are shown. For the sake of completeness, raw data are shown in Appendix A.

Let us start by taking the case $\mu_s = 0.5$ as an example. The relative viscosity has been interpolated at selected values of volume fraction and shear stress, forming a grid, and using a cubic 2D interpolation. A logarithmic scale has been chosen for both η^s and σ^*. In Fig. 8, an interpolation of η^s over a very fine grid (ϕ, σ^*) is shown to evidence the double dependence of the relative viscosity on the volume fraction and the shear stress. For quantitative processing and to guarantee the accuracy of the interpolated data, values of ϕ and σ^* have been selected close to the raw ones, on a coarse-grained grid. The interpolated values are displayed in Fig. 9 and are compared with raw data. In Fig. 9 [top], where the reduced shear stress is displayed as a function of reduced shear rate, we can appreciate the yield stress behavior, even though a yield stress is difficult to quantitatively determine due to the lack of data in the low-reduced-shear-rate range. Molecular dynamic simulations of frictionless particle suspensions[3] have evidenced a specific regime between the stress plateau at low shear rate and the Newtonian regime at high shear rate, where the stress increases weakly with the shear rate, defining a shear-thinning response with a sublinear power law. This regime has been attributed to clusters whose size would decrease as stress increases. In the present case, where we cannot probe the low-shear-rate range, such a regime is difficult to address. We can also appreciate the well-known effect of the volume fraction: for the same shear rate $\dot{\gamma}$, a higher shear stress σ^* is obtained for a higher volume fraction ϕ; in addition, we can foresee that the extrapolated value of the shear stress at zero shear rate (i.e., the yield stress) increases with ϕ. In Fig. 9 [bottom], the relative viscosity is displayed for different values of the shear stress as a function of volume fraction, evidencing that the maximum volume fraction ϕ^{μ}_{m} decreases as σ^* decreases.

The procedure described above would be less accurate for the cases with $\mu_s = 0.1$ and $\mu_s = 0$ because the raw data are far from forming an even grid in the plane (ϕ, σ^*). This is why we performed a linear interpolation of both $\log(\eta^s)$ and ϕ, separately, at selected values of $\log(\sigma^*)$, the latter being chosen close to the raw data to increase the accuracy of the interpolation. It should be noted that for each interpolated point in the 3D space $(log(\sigma^*), \phi, \log(\eta^s))$, this procedure uses only two raw data points, which justifies this double linear interpolation. For the sake of consistency, we re-interpolated the data for $\mu_s = 0.5$ with this procedure, choosing the same values for σ^* as in Fig. 9. The interpolation results are proposed in Fig. 10, where a comparison with raw data is shown. It should be noted that the interpolated values for $\mu_s = 0.5$ are closer to the raw data, with the drawback however that the interpolation is not performed at predefined values of the volume fraction.

Based on the results, we can define a stress-dependent maximum volume fraction $\phi^{\mu}_{\text{m}}(\sigma^*)$ to model the variation of the viscosity with the volume fraction. This description of an adhesive suspension has already been proposed by other works[7–9,33,69]. The maximum volume fraction ϕ^{μ}_{m} corresponding to a given value of the shear stress σ^* is obtained by fitting an appropriate function to the data. This procedure is a bit tricky, since the available data, including interpolated values, are scarcer in the low-volume-fraction and low-stress range. In more detail, a stress-dependent Maron-Pierce law is fitted

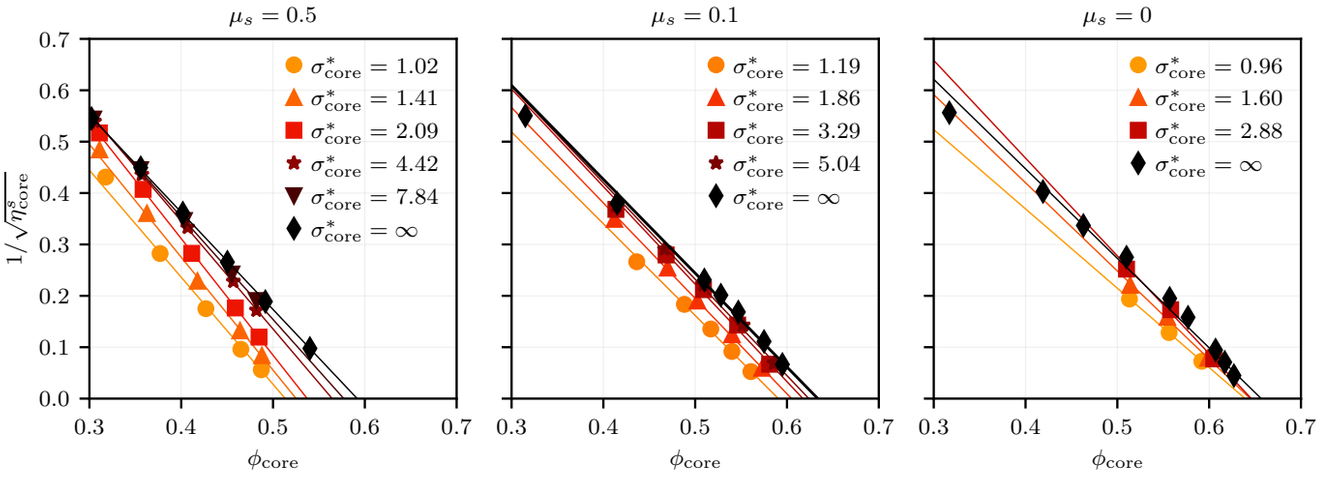

FIG. 11. Constant stress interpolated data, together with the best fit of the Maron-Pierce law (Eq. (23)). (⧫): non-adhesive particles data from the present simulations ($\mu_s = 0.5$), data by Gallier, Peters, and Lobry [68] ($\mu_s = 0$), and unpublished data by Stany Gallier ($\mu_s = 0.1$).

at constant σ^*:

$$\eta^s = \frac{\alpha(\sigma^*)}{\left(1 - \dfrac{\phi}{\phi^{\mu}_{\rm m}(\sigma^*)}\right)^2}, \tag{23}$$

where α and $\phi^{\mu}_{\rm m}$ are free parameters, whose evolution with σ^* is investigated in the following.

The interpolated data together with the fitting function – Eq. (23) – are displayed in Fig. 11. At high shear stress the non-adhesive particle suspension viscosity is recovered, and the lower the shear stress, the lower the maximum volume fraction. The latter behavior is less and less pronounced when decreasing the friction coefficient. At $\mu_s = 0$, the maximum volume fractions seems to weakly change in the probed stress range. However, adhesion still clearly increases the viscosity.

Another peculiar behavior can be observed for $\mu_s = 0$: at high volume fractions the viscosity diverges more rapidly, losing the linearity of $1/\sqrt{\eta^s}$ with ϕ (it is very clear in the non-adhesive results by Gallier, Peters, and Lobry [68]). As a consequence, at low-to-medium volume fractions the viscosity is conveniently described by the Maron-Pierce law with a quite high extrapolated maximum volume fraction, while at high volume fractions ($\phi \gtrsim 0.5 - 0.55$) a faster divergence is observed. This explains in particular why simulations of moderately concentrated suspensions of frictionless particles ($\phi \lesssim 0.55$) yield a jamming fraction of around 0.7 instead of 0.64-0.65[45,66]. This trend is absent for $\mu_s = 0.5$, for which a linear dependence between $1/\sqrt{\eta^s}$ and ϕ holds over the whole data range investigated. In the case of $\mu_s = 0.1$, this dual behavior of the viscosity is visible at high stresses and in the non-adhesive particle suspensions. It should be noted that the values of $\phi^{\mu}_{\rm m}$ without adhesion for $\mu_s = 0$ and $\mu_s = 0.1$ shown in Fig. 15 have been computed by fitting η^s at $\phi \geq 0.45$. We also note that a better agreement between measurement and correlation law has been found before for frictionless particles over a large volume fraction range by allowing the power exponent in Maron-Pierce law to take a value lower than 2 (approximately 1.6)[13,68,70].

Finally, as already mentioned, for $\mu_s = 0$ (and to a lesser extent $\mu_s = 0.1$), the relative viscosity varies less with the shear stress compared to suspension of high friction particles. This could suggest that σ^* has not been decreased enough. On the other hand, a strong increase in the core volume fraction is observed, suggesting the inception of shear-banding.

2. *FCM simulations*

The FCM data is easier to process, since the volume fraction is imposed and homogeneous, at least as long as shear-banding does not occur, which still happens at low stress for $\phi \leq 0.4$. A simple interpolation at preset values of the reduced stress is required, allowing to determine the fitting parameters

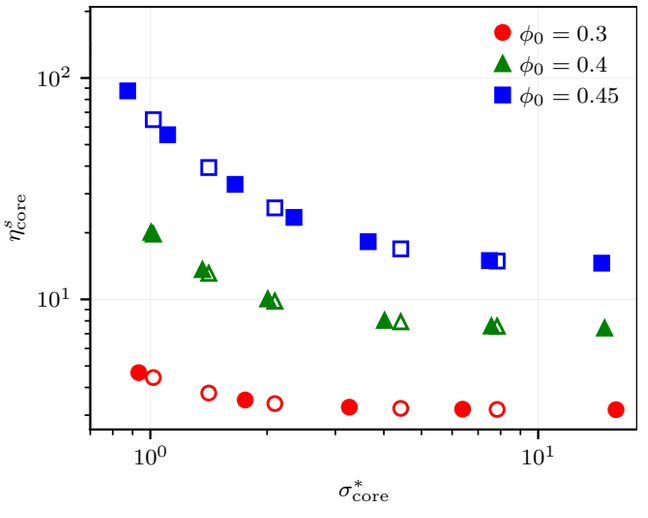

FIG. 12. Relative shear viscosity from FCM simulations. $\mu_s = 0.5$. Solid symbols: raw data. Open symbols: interpolated data.

$[\alpha(\sigma^*),\ \phi_{\rm m}^{\mu}(\sigma^*)]$. This is illustrated in Fig. 12, where the viscosity at $\mu_s = 0.5$ is interpolated at the same values of the reduced stress as in Fig. 10 (right column). The interpolated viscosity is compared with the one obtained with the FDM in Fig. 13, showing again a good agreement.

Finally, to conclude on the relevance of Eq. (23), all the interpolated viscosities are displayed in Fig. 14 as a function of $\phi/\phi_{\rm m}^{\mu}(\sigma^*)$, where each curve corresponds to a given value of σ^*. All data collapse reasonably well, with a residual dispersion due to the variation of $\alpha(\sigma^*)$ between 0.65 and 1 (Appendix C, Fig. 32).

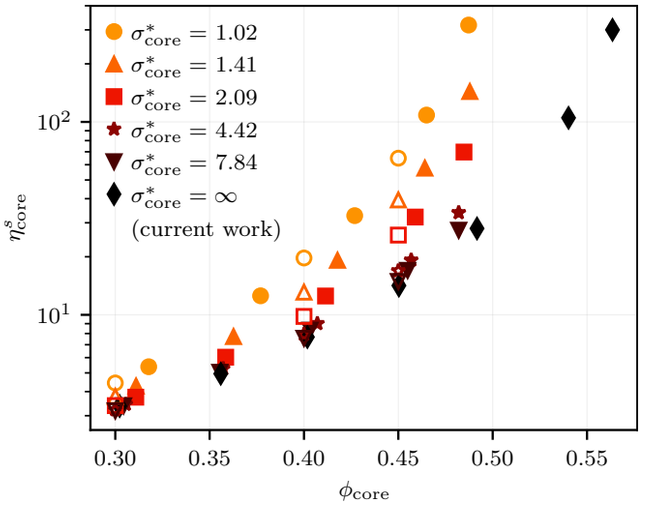

FIG. 13. Viscosity at $\mu_s = 0.5$ computed with the FDM (solid symbols) and with the FCM (open symbols)

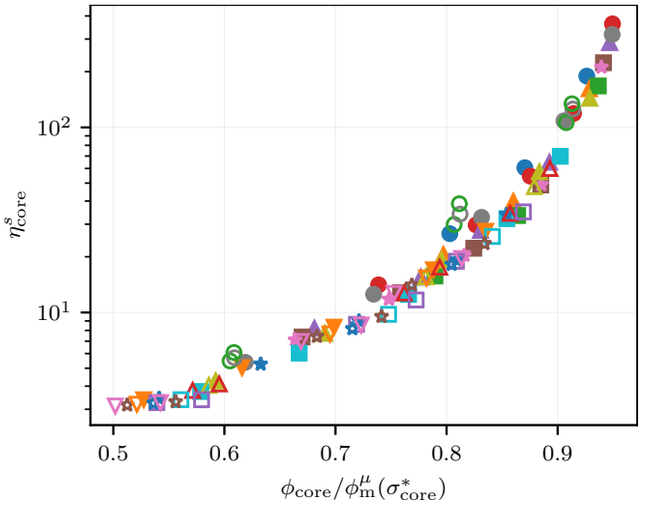

FIG. 14. Relative viscosity $\eta^s_{\rm core}$ of adhesive particles suspensions as a function of reduced volume fraction $\phi/\phi_{\rm m}^{\mu}(\sigma^*_{\rm core})$ for all simulations. Interpolated data from FCM (open symbols) and FDM (solid symbols) simulations. $\sigma^*_{\rm core} \in [0.7, 10]$.

3. *maximum volume fraction and yield stress*

In Fig. 15, the curves $\phi_{\rm m}^{\mu}(\sigma^*)$ are displayed for different values of the friction coefficient. We recall that each curve in the plane $(\sigma^*,\ \phi)$ has been built using constant stress and friction coefficient data under the curve (Fig. 10). In other words, it splits the plane into a flowing region (under the curve), and a jammed region (above the curve). However, each point in the same transition curve could be approached at constant volume fraction ϕ, from the right, so that the considered point would define the concentration-dependent yield stress $\sigma_Y(\phi)$[8,9].

We appreciate a good agreement for $\mu_s = 0.5$ between FCM and FDM. This has to be considered a supplementary validation because, as already pointed out, in the FCM simulations, the product $\dot{\Gamma} \times G_0^{adh}$ has been kept constant: this has not been done in the FDM simulations and the same results are obtained; therefore, it can be assumed that there is no influence of this choice in the scope of the present study.

Fig. 15 deserves a few comments. First, the maximum volume fraction increases as the reduced stress increases, and levels off to its non-adhesive value. Since the same figure displays the evolution of the yield stress as a function of the volume fraction – as implied by Eq. (23) – it means that the yield stress increases with the volume fraction, and diverges as the non-adhesive maximum volume fraction is approached.

Concerning the effect of friction, the high-stress limit of the maximum volume fraction decreases as the friction coefficient increases, as already known from simulations of non-adhesive particle suspensions. For high-enough a friction coefficient ($\mu_s \geq 0.3$), the maximum volume fraction converges toward a single value as the reduced stress decreases to $\sigma^* \approx 0.6 - 0.7$, showing that the influence of strong friction on the maximum

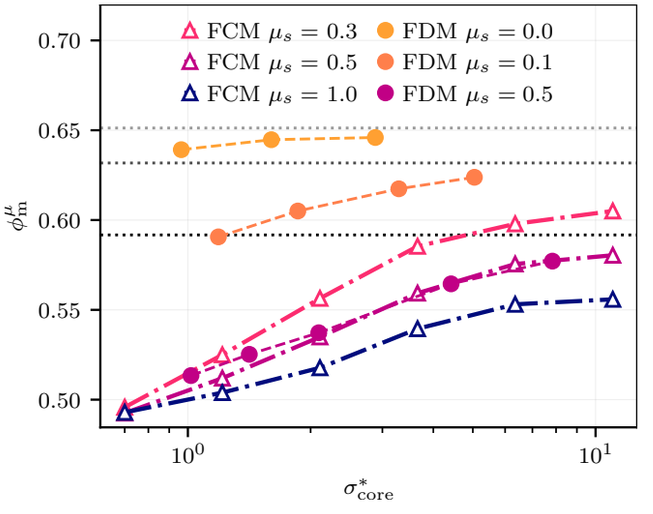

FIG. 15. $\phi_{\rm m}^{\mu}(\sigma^*_{\rm core})$: results obtained with the FDM (triangles) and the FCM (bullets). The horizontal dotted gray lines are the maximum volume fractions in the non-adhesive case from FDM simulations ($\sigma^*_{\rm core} = \infty$): (lower line) data from Orsi [39] ($\mu_s = 0.5$, $\phi_{\rm m}^{\mu} = 0.592$), (center line) unpublished data by Stany Gallier ($\mu_s = 0.1$, $\phi_{\rm m}^{\mu} = 0.632$), and (upper line) Gallier, Peters, and Lobry [68] ($\mu_s = 0$, $\phi_{\rm m}^{\mu} = 0.651$); the results by Stany Gallier have been fitted for $\phi_{\rm core} \geq 0.45$.

volume fraction decreases when increasing the adhesive force. On the other hand, the overall effect of adhesion seems less pronounced at lower friction coefficients. Again, this last assertion is to be somewhat softened since shear-banding is still observed, which impedes probing the low-stress range.

D. Contribution of the contact forces to the stresses

In the previous section, it has been shown shown that the shear stress developing in frictional adhesive particle suspensions can be understood within the same modeling framework as for non-adhesive particle suspensions, providing that the usual maximum volume fraction now depends on the shear stress. The question arises, whether the same statement holds for other quantities than shear stress, which issue will be addressed in the following sections. For the sake of simplicity, we mainly focus on the case $\mu_s = 0.5$, at least for the adhesive particle suspensions.

1. *Reduced second normal stress*

Fig. 16 displays the reduced second contact normal stress, $\hat{\Sigma}^c_{22} = \Sigma^c_{22}/\Sigma^s_{12}$ as a function of volume fraction [top] and the reduced volume fraction $\phi/\phi^\mu_{\rm m}$ [bottom] for non-adhesive suspensions with different values of the friction coefficient (data from FCM simulations[6]). This quantity is essentially the quantity $q(\phi)$ defined and plotted by Morris and Boulay [64] and shown to be important in describing migration phenomena. Later work, e.g Boyer, Guazzelli, and Pouliquen [71], used it in the inverted form of a bulk friction coefficient in the now widely adopted $\mu(J)$ formulation of suspension rheology. This latter perspective is further explored in the context of adhesive particles in Section III E. As usual, the contact normal stresses are compressive. Friction increases $|\hat{\Sigma}^c_{22}|$ – Fig. 16 [top] – and all the data collapse on the same master curve if displayed as a function of reduced volume fraction – Fig. 16 [bottom]. This latter behavior has already been implicitly evidenced in frictional suspensions, except for frictionless or low-friction particles[70]. Although not displayed, the same behavior holds for other contact normal stresses. Thus, $\hat{\Sigma}^c_{22}$ may be considered an indicator of how close the suspension is to the jammed state, as is η^s, independently of the friction coefficient, provided the latter is not too low.

The same rationalization does not hold anymore for frictional adhesive suspensions. As displayed in Fig. 17 [top] for a friction coefficient $\mu_s = 0.5$, adhesion hardly changes $\hat{\Sigma}^c_{22}$. This is highlighted in Fig. 17 [bottom], where the same quantity is displayed as a function of reduced volume fraction $\phi/\phi^\mu_{\rm m}(\sigma^*)$. In that case, for a given value of μ_s, decreasing σ^* drives the suspension toward the jammed state (see Section III C), but without strongly affecting $\hat{\Sigma}^c_{22}$. We note that this behavior is observed both in the high- and low-volume fraction ranges. Splitting the ratio $\hat{\Sigma}^c_{22} = \Sigma^c_{22}/\Sigma^s_{12}$ into $\Sigma^c_{12}/\Sigma^s_{12} \times \Sigma^c_{22}/\Sigma^c_{12}$ may help to understand this trend, as explained in the following.

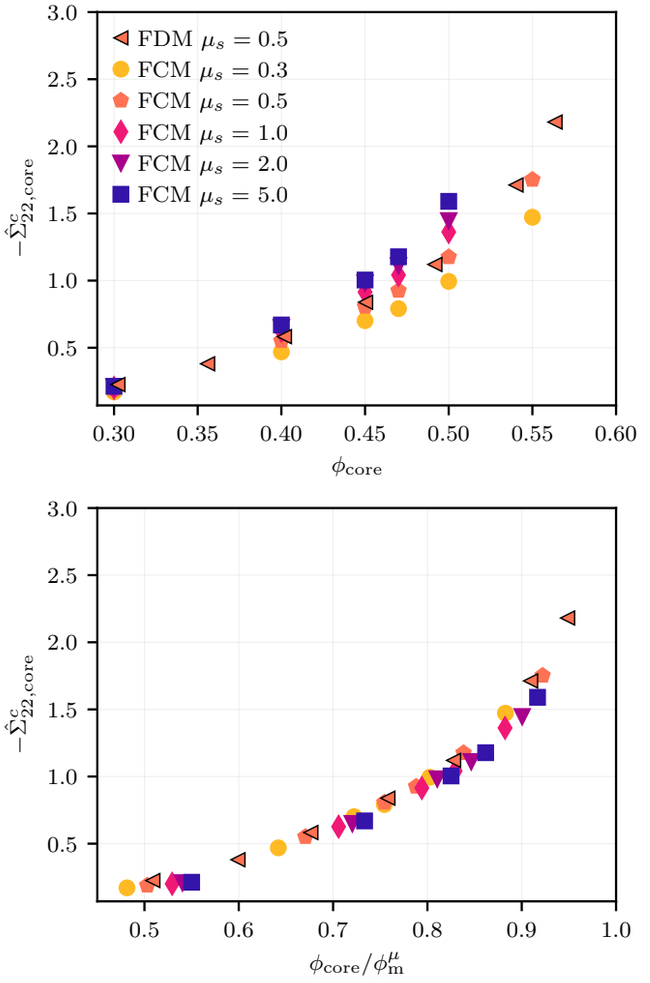

FIG. 16. Reduced contact stress $-\hat{\Sigma}^c_{22,\rm core} = -\Sigma^c_{22,\rm core}/\Sigma^s_{12,\rm core}$ as a function of volume fraction for different values of the friction coefficient μ_s for suspensions of non-adhesive particles.

2. *Contribution of the contact forces to the tangential stress*

The relative contribution of the contact forces to the total shear stress, $\Sigma^c_{12}/\Sigma^s_{12}$, in non-adhesive frictional suspensions only depend on the reduced volume fraction, $\phi/\phi^\mu_{\rm m}$, whatever the value of the friction coefficient, provided it is not too low, as shown in Fig. 18. We note that an approximation to this master curve may be measured in shear reversal experiments[72].

This master curve is illustrated in Fig. 19 for $\mu_s = 0.5$ (black triangles). The interpretation is straightforward: as the suspension gets closer to the jammed state, the contribution of the contact forces to the shear stress becomes predominant, and $\Sigma^c_{12}/\Sigma^s_{12}$ tends to 1 as ϕ approaches $\phi^\mu_{\rm m}$. In Fig. 19, the data corresponding to the adhesive particle suspensions is also displayed. As expected, a strong effect of adhesion is observed: reducing the stress increases $\Sigma^c_{12}/\Sigma^s_{12}$ – Fig. 19 [top] – which is qualitatively consistent with the progress toward the jammed state. In Fig. 19 [bottom], the interpolated data

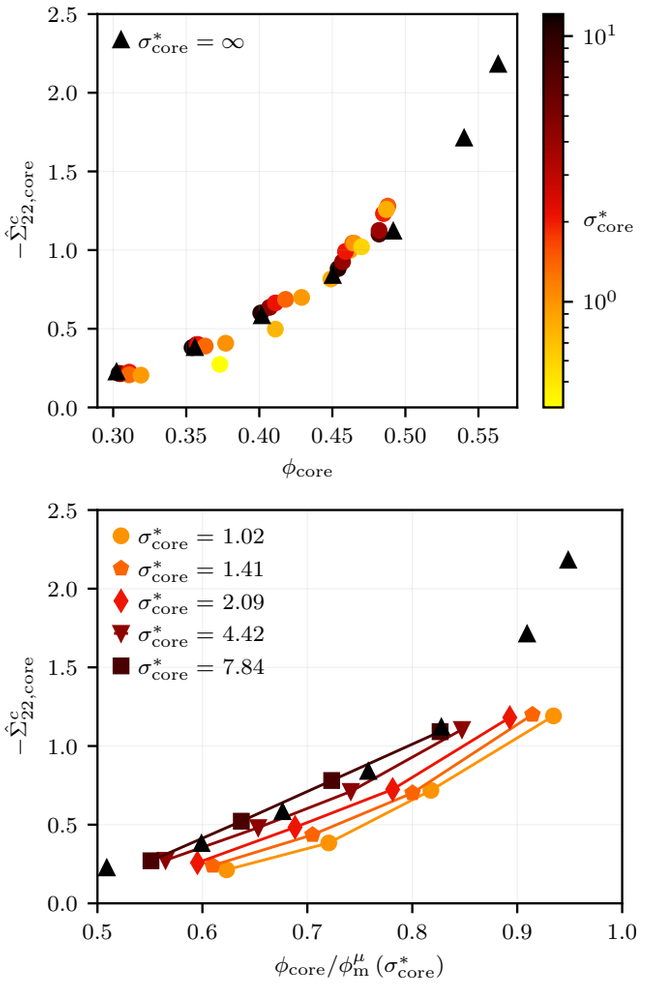

FIG. 17. Reduced contact stress $-\hat{\Sigma}^c_{22,\text{core}} = -\Sigma^c_{22,\text{core}}/\Sigma^s_{12,\text{core}}$ as a function of volume fraction for different values of the reduced stress σ^*_{core}. $\mu_s = 0.5$. Left: raw data. Right: interpolated data.

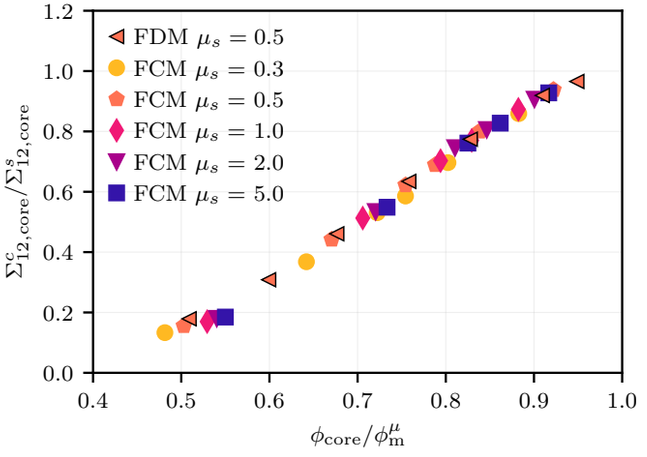

FIG. 18. Reduced contact stress $\Sigma^c_{12,\text{core}}/\Sigma^s_{12,\text{core}}$ as a function of volume fraction for different friction coefficients μ_s. $G^{adh}_0 = 0$.

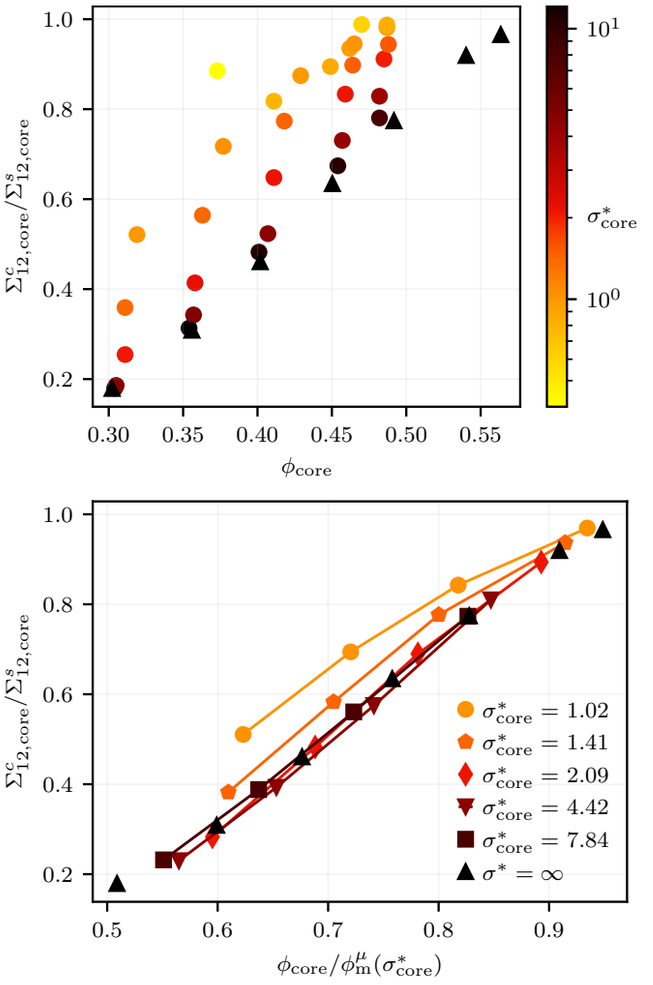

FIG. 19. Reduced contact tangential stress $\Sigma^c_{12,\text{core}}/\Sigma^s_{12,\text{core}}$ as a function of volume fraction for different values of the reduced stress σ^*_{core}. $\mu_s = 0.5$. Left: raw data. Right: interpolated data.

approximately collapse on the same master curve when displayed as a function of the reduced volume fraction, with significant discrepancy at low volume fraction and low stress, where the relative contribution of contact forces is higher than expected. At higher volume fraction ($\phi \gtrsim 0.45$, high range of each constant stress curve in Fig. 19 [bottom]) on the contrary, the data approximately collapse on the master curve for the non-adhesive suspension.

3. *Relative intensity of normal and tangential contact stresses*

The ratio of the contact normal stresses to their tangential counterpart is now addressed. We focus on the normal stresses in the shear plane. In non-adhesive particle suspension first, in Fig. 20, the ratios $\Sigma^c_{ii}/\Sigma^c_{12}$ $(i = 1, 2)$ are shown to roughly collapse on the same curve when displayed against the reduced volume fraction. In the considered volume fraction range $\phi/\phi^\mu_{\text{m}} \in [0.5, 0.95]$, they are of similar value, around $1-2$. At

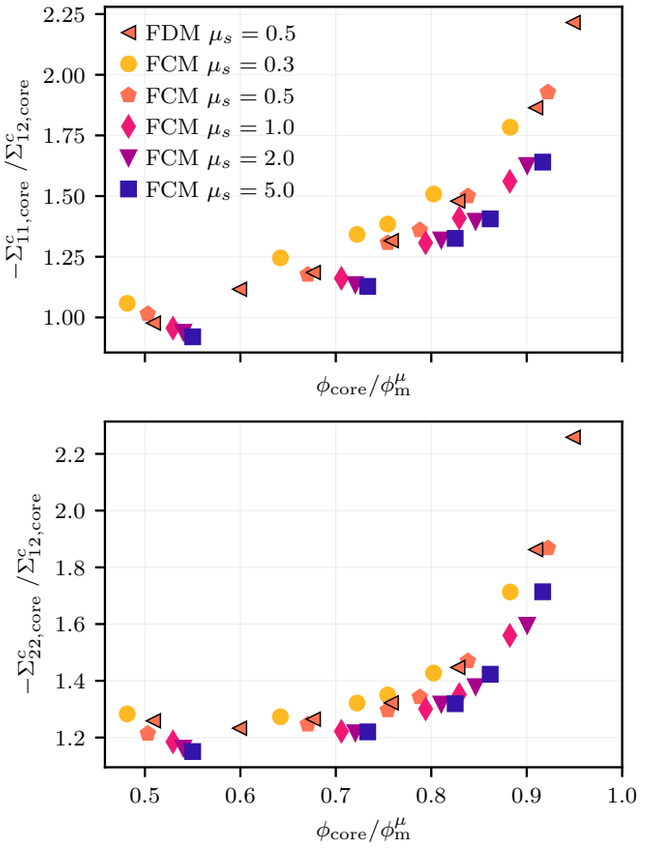

FIG. 20. Ratio of the normal to tangential contact stresses as a function of volume fraction for friction coefficients μ_s. $G_0^{adh} = 0$.

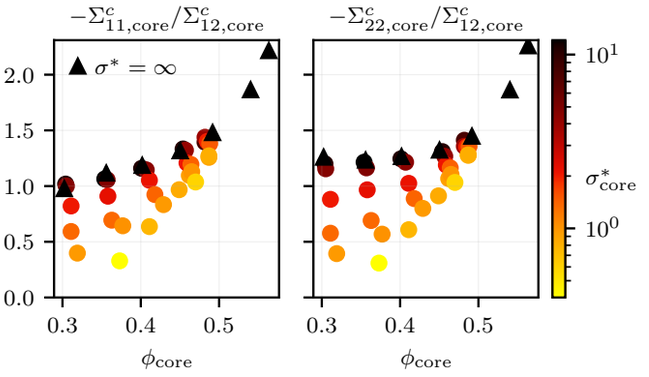

FIG. 21. Ratio of the normal to tangential contact stresses as a function of volume fraction for different values of the reduced stress σ^*_{core}. $\mu_s = 0.5$. Left: raw data. Right: interpolated data.

moderate volume fraction $\phi/\phi^\mu_{\mathrm{m}} \approx 0.5$, the values of both the contact normal stresses are close to their tangential counterpart, while their relative importance softly increases with the reduced volume fraction up to around 2 at $\phi/\phi^\mu_{\mathrm{m}} \approx 0.95$. Overall, this means that the structure of the contact stress tensor slowly evolves over the probed volume fraction range, with an increasing relative intensity of the normal stresses as the jammed state is approached.

Adhesive forces tend to decrease the considered ratio for both normal stresses, mostly in the low-volume-fraction range (Fig. 21). The influence of adhesion in that perspective is very weak at $\phi \sim 0.48$ – Fig. 21 – even though the suspension is driven significantly closer to the jammed state – Fig. 19 [bottom] and Fig. 10 – which trend still contrasts with non-adhesive particle suspensions that would show an increase of the ratios upon approaching the jammed state, instead of a weak decrease. From Fig. 21, the same feature is expected for higher volume fractions, although this more concentrated range was not addressed. In the low-volume-fraction range, however, adhesion strongly decreases the relative intensity of the contact normal stresses. At the lowest volume fraction probed around 0.3 for the lowest considered stress (before shear-banding occurs), the contact stress tensor $\boldsymbol{\Sigma}^c$ in the shear plane is nearly a pure shear stress tensor, with low isotropic pressure. Since this strong decrease of the contact pressure relative to the stress intensity ends with the inception of shear-banding, it may be involved in the mechanism that drives this instability, which may deserve further studies. Finally, a qualitative microscopic picture of this behavior will be proposed in Section III F.

As a conclusion, adhesive and non-adhesive particle suspensions may behave quite differently as the jammed state is approached, from the perspective of contact normal stresses. In the latter case, the ratio $\hat{\Sigma}^c_{22} = \Sigma^c_{22}/\Sigma^s_{12}$ depends on $\phi/\phi^\mu_{\mathrm{m}}$ and its intensity increases as the reduced volume fraction increases. In the former case, the jammed state may be approached at constant volume fraction through stress decrease, i.e., decrease of $\phi^\mu_{\mathrm{m}}(\sigma^*)$, with basically no change in $\hat{\Sigma}^c_{22}$. In that case, the relative contribution of contact forces to the tangential stress, $\Sigma^c_{12}/\Sigma^s_{12}$, increases (Section III D 2), while the contact normal stresses, Σ^c_{ii} , decrease relative to the corresponding tangential component, Σ^c_{12}, (Section III D 3), which is indeed consistent with the weak variation of $\Sigma^c_{22}/\Sigma^s_{12}$. These behaviors are not rationalized when displayed against the reduced volume fraction $\phi/\phi^\mu_{\mathrm{m}}(\sigma^*)$. According to Section III D 3, the structure of the contact stress tensor is strongly altered in the low-volume-fraction range, with an increasing predominance of the contact shear stress over the contact normal stresses.

E. Macroscopic friction coefficient μ

The so-called $\mu(J)$ formulation of non-Brownian suspension rheology, which was initially developed in dry granular physics, has proven powerful in the field of non-adhesive particle suspension. The apparent friction coefficient and the viscous number are respectively defined as $\mu = -\Sigma^s_{12}/\Sigma^c_{22}$ and $J = -\eta\dot{\gamma}/\Sigma^c_{22}$. In adhesive particle suspensions, the usual description $(\mu = \mu(J), \phi/\phi_J = f(J))$[66,70] is expected not to hold anymore, due to a new stress scale $F^{adh}/(6\pi a_1^2)$, as already shown in cohesive granular rheology[73,74]. Here, data $\mu_s = 0.5$ is shown.

Fig. 22 [left] displays the variation of the apparent friction coefficient as a function of the viscous number for differ-

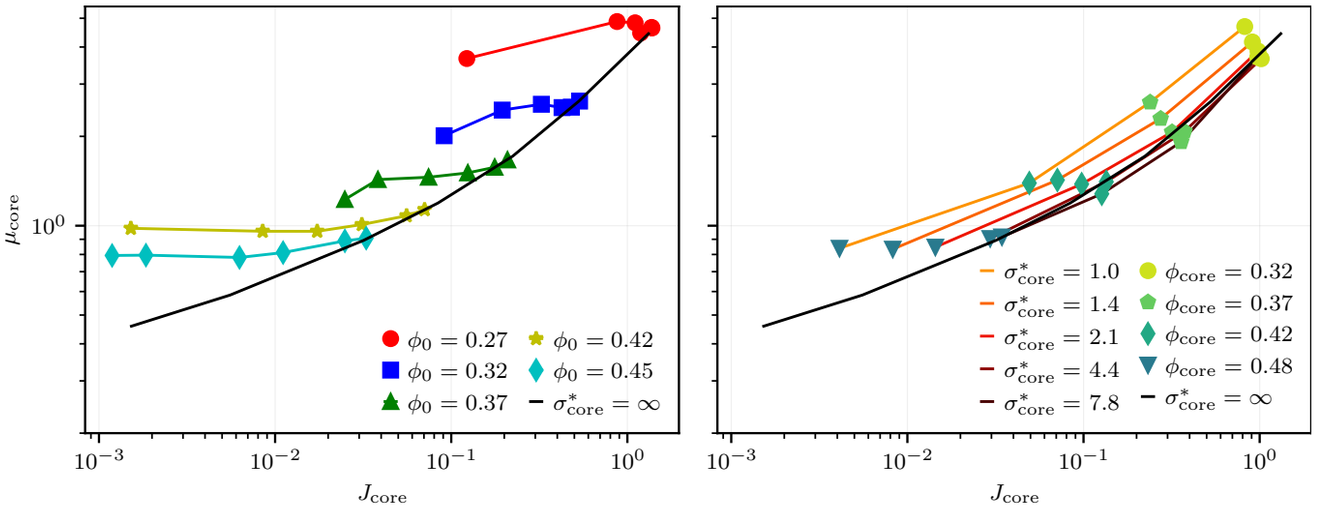

FIG. 22. Variation of the apparent friction coefficient as a function of viscous number from FDM simulations ($\mu_s = 0.5$). Left: raw data for various values of the mean volume fraction ϕ_0. The reduced shear stress $\sigma^*_{\rm core}$ decreases as the data points move away from the infinite-stress curve. Right: data interpolated at constant volume fraction and reduced stress.

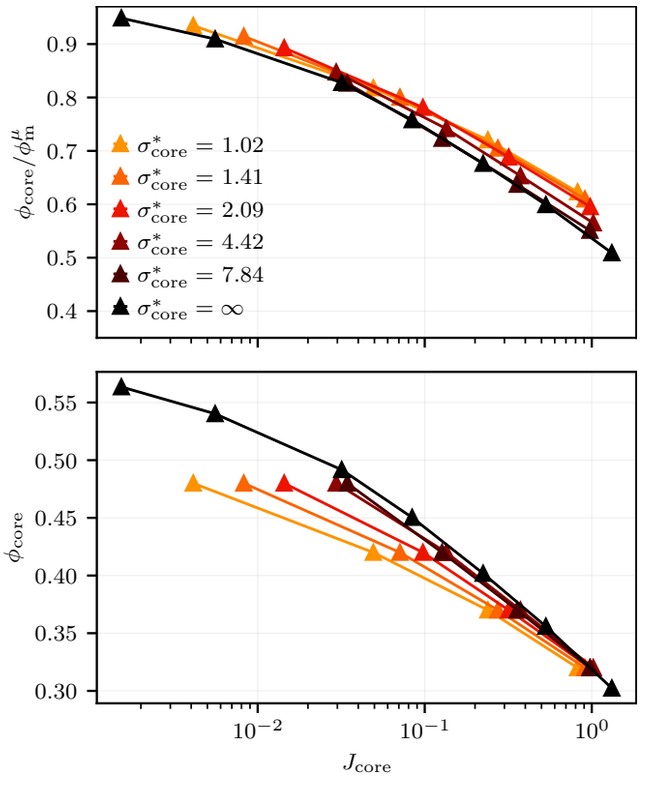

FIG. 23. Volume fraction as a function of viscous number for different reduced stresses $J_{\rm core}$ (interpolated data, $\mu_s = 0.5$). Top: reduced volume fraction $\phi_{\rm core}/\phi^\mu_{\rm m}(\sigma^*_{\rm core})$. Bottom: volume fraction $\phi_{\rm core}$.

ent mean volume fractions ϕ_0 and for varying reduced stress. From a qualitative perspective, as the reduced stress is decreased, the viscous number decreases as well, while the variation of μ is quite weak. More specific comments are made difficult by the underlying variation of the volume fraction with the stress, and also since the data is not sampled at predefined stress, as already noted. A clearer picture is given by Fig. 22 [right], which displays the same data interpolated at constant volume fraction and stress. As the reduced stress is decreased, the constant-stress curves are positively shifted, so that for a given value of the viscous number J, the apparent friction coefficient μ increases. In Fig. 22 [right], data points corresponding to a given volume fraction are consistently colored across all constant σ^* curves. This representation clearly demonstrates that μ is primarily a function of the volume fraction, at least in the high-volume-fraction range, as already evidenced in Fig. 17. Regarding the volume fraction (Fig. 23), a better collapse of the curves is obtained when considering the reduced volume fraction $\phi/\phi^\mu_{\rm m}(\sigma^*)$, as observed in frictional non-adhesive suspensions[70]. As a consequence of the latter observation, at constant viscous number, the volume fraction decreases when decreasing the reduced stress (Fig. 23 [bottom]). All these behaviors are in qualitative agreement with simulations of dry cohesive granular materials in two-dimensional[73] and three-dimensional[74] systems.

As expected, the data do not collapse in the plane (J,μ). This may also be understood in the high-concentration range from the previous sections using the relation $1/J = -\eta^s \times \hat{\Sigma}^c_{22}$. As σ^* is decreased at constant volume fraction, η^s diverges, while $\hat{\Sigma}^c_{22}$ is quite constant so that J tends to zero and $\mu = -1/\hat{\Sigma}^c_{22}$ weakly changes.

Meanwhile, η^s is mostly a function of $\phi/\phi^\mu_{\rm m}(\sigma^*)$ while $\hat{\Sigma}^c_{22}$ mostly depends on ϕ. As a consequence, no real master curve is found in the plane $(J,\phi/\phi^\mu_{\rm m})$, even though no strong dispersion is observed either.

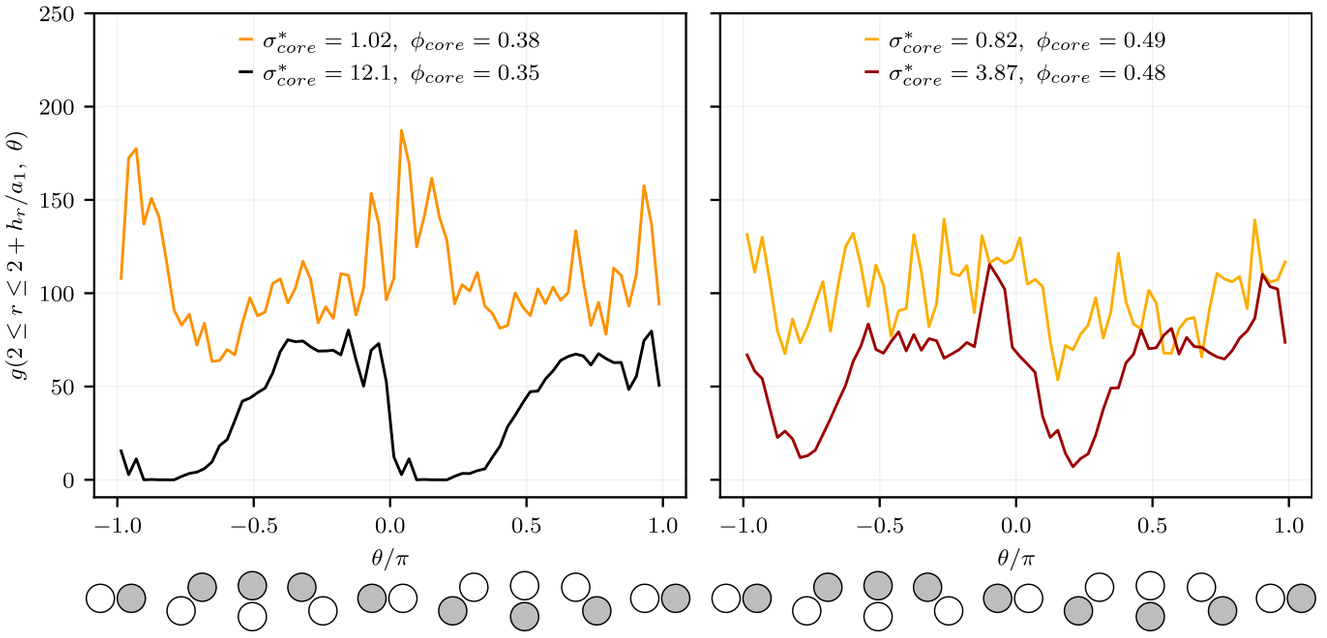

FIG. 24. Pair distribution function at contact $r/a_1 \in [2, 2.005]$ as a function of position angle: [left] for $\phi_0 = 0.32$ at high ($G_{adh} = 7.3$, $\sigma^* = 1.02$) and low ($G_{adh} = 0.96$, $\sigma^* = 12.1$) adhesive force, and [right] for $\phi_0 = 0.45$ at high ($G_{adh} = 377$, $\sigma^* = 0.82$) and low ($G_{adh} = 6.54$, $\sigma^* = 3.85$) adhesive force. For clarity, the particle pair orientation associated with the indicated angle is illustrated beneath the x-axis; the grey-filled circle denotes the reference particle.

F. Adhesive particle suspension microstructure

The distribution of contact pairs is now shortly discussed. It is well known that the rheological behavior of frictional non-Brownian suspensions is closely related to the shear-induced microstructure (see Morris [75], Guazzelli and Pouliquen [76] for reviews on the subject). The latter is usually characterized by the pair distribution function (PDF), i.e., the probability to find a particle at a given position relative to a reference particle. We are interested in the PDF of contacting particles. For the sake of simplicity, we only consider a pair of particles with radius a_1 in the shear plane.

The pair distribution at contact averaged over $r \in [2, 2 + h_r/a_1]$ is displayed in Fig. 24 [left] for a suspension with mean volume fraction $\phi_0 = 0.32$ and in Fig. 24 [right] for $\phi_0 = 0.45$, at two values of the reduced stress. $\phi_0 = 0.32$ was chosen since shear-banding is observed at low stress (lower than the values considered here, though). The volume fraction in the core of the suspension increases as the stress decreases, as previously discussed. The angle θ is measured from the flow direction, $\theta = [-\pi/2, 0]$ and $[\pi/2, \pi]$ corresponding to the compressional quadrant of the shear flow. At high stress, the PDF displays the usual feature found in moderately concentrated suspension, i.e., a high probability of contacting pair in the compressional quadrant and a depletion of particles in the extensional one[77]. The interaction forces are mostly compressive and frictional, with weak influence of the adhesive force, so that contacting pairs are formed in the compressional quadrant, and split up as they are driven into the extensional quadrant. At low stress, the PDF offers a quite different picture, where the depletion area is basically lacking, and the contacting pairs are approximately isotropically distributed. The mean value of the PDF is significantly larger compared to the high-stress limit, meaning that the number of contacts per particle is larger, too. A basic explanation is straightforward: at this low stress value, the adhesive force has a strong influence on the particle motion. Specifically, it works against the flow in the extensional quadrant, keeping particles in contact.

Additional insight is provided by Figs. 25 and 26, where the distribution of normal contact forces at the reference particle surface ($2 \leq r \leq 2 + h_r/a_1$) is displayed at the same volume fraction and stress values as in Fig. 24. It should be noted that the length of the arrow cannot be compared between different sets of parameters, but only between the different contributions (elastic, adhesive, or total) of the same case. In the frame of the present model, the normal contact force is the sum of a constant attractive force (toward the outside of the reference particle) and an elastic repulsive force (toward the inside of the particle), allowing to formally separate both contributions in Figs. 25 and 26, respectively [center] and [left]. Focusing first on the low volume fraction and low stress case, Fig. 25 [top], the approximately isotropic distribution of pairs is reflected in the same property of the adhesive force contribution. The repulsive elastic force is more intense in the compressional quadrant where the mean shear flow drives the particles into contact, and weaker in the extensional quadrant, where the mean shear flow tends to separate them. This results in a quadrupolar distribution of the total force – Fig. 25 [right] – where the particle pairs in the compressional (respectively extensional) quadrant experience compressive (respectively

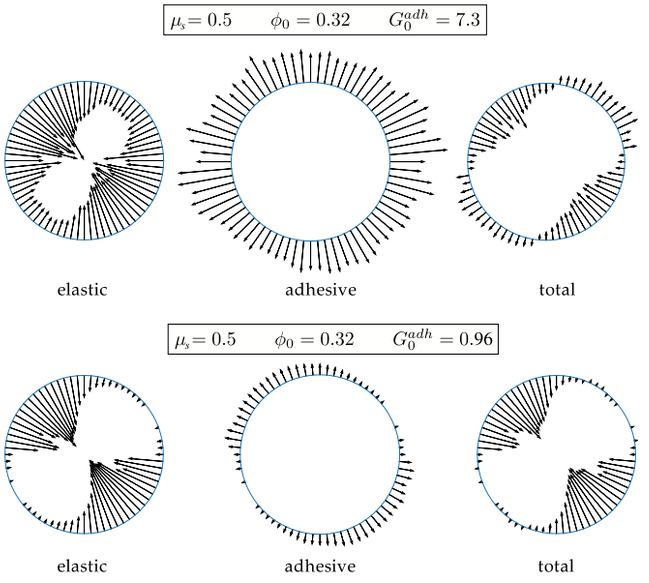

FIG. 25. Distribution of the normal contact forces on the surface of the particles for a moderately concentrated case ($\phi_0 = 0.32$) at two values of the reduced stress ($G_0^{adh} = 7.3; \sigma^* = 1.02$ [top], and $G_0^{adh} = 0.96; \sigma^*_{\text{core}} = 12.1$ [bottom]). Comparison between the distribution of the elastic [left] and adhesive [center] contributions to the total contact normal force [right]. $\mu_s = 0.5$.

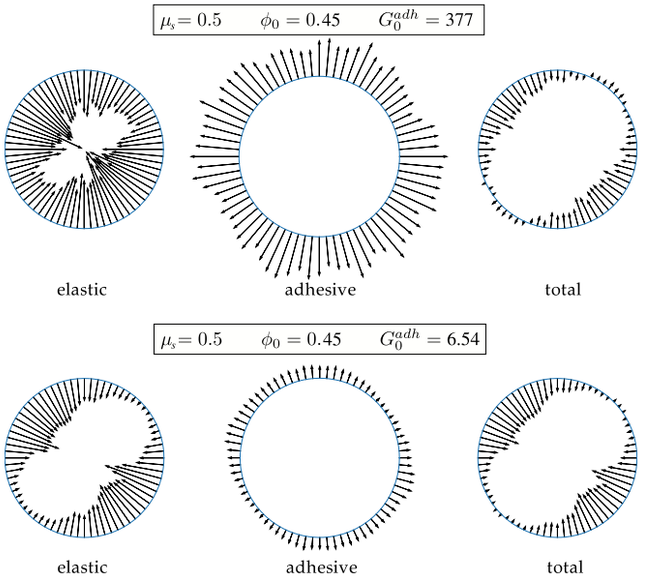

FIG. 26. Distribution of the normal contact forces on the surface of the particles for a moderately concentrated case ($\phi_0 = 0.45$) at two values of the reduced stress ($G_0^{adh} = 377; \sigma^* = 0.82$ [top], and $G_0^{adh} = 6.54; \sigma^*_{\text{core}} = 3.87$ [bottom]): comparison between the distribution of the elastic [left] and adhesive [center] contributions to the total contact normal force [right]. $\mu_s = 0.5$.

tensile) forces. At high stress (Fig. 25 [bottom]), due to the relatively weaker adhesive force, the particle depletion in the extensional quadrant develops, and the total force distribution lacks the tensile part. It should be noted that the quadrupolar force distribution at low stress is clearly responsible for the weakening of the normal contact stresses and of the normal contact pressure in the shear plane, compared to the tangential contact stress (Fig. 21). Interestingly, we observe that the adhesive contribution in the extensional quadrant is significantly weaker at high volume fraction (Fig. 26 [top,right]), even though the PDF at contact displays similar isotropic distribution, resulting in a contact force distribution similar at low and high stress (Fig. 26 [right], respectively [top] and [bottom]). This latter feature is consistent with the weak variation with σ^* of the reduced normal stresses $\Sigma^c_{ii}/\Sigma^c_{12}$ at this volume fraction observed in Fig. 21. Finally, this qualitative discussion is only based on the normal contact forces, to the exclusion of the friction forces, which is qualitatively valid, since we checked that the shear stress directly originating in friction forces amounts to 30% at most of the total contact shear stress, similar to non-adhesive particle suspensions ($\approx 25\%$[45]). In addition, the direct contribution of friction forces to the total contact normal stresses in the plane of shear keeps under 6%.

IV. DISCUSSION AND PERSPECTIVES

The definition of a stress-dependent maximum volume fraction – $\phi_m^\mu(\sigma^*)$ – has already been proposed to describe the yield stress of adhesive particle suspensions[7,69]. More recently, Richards *et al.*[8] were able to interpret experimental viscosity data of an adhesive suspension by adapting the so-called "constraint rheology" model proposed by Guy, Hermes, and Poon[31]. The authors were able to define, in the phase space (ϕ, σ^*), a flowing region and a jammed region, separated by a $\phi_m^\mu(\sigma^*)$ curve similar to those we have evidenced. In their case, they reach much lower volume fractions, of the order of ≈ 0.35 (≈ 0.20 in the work by Richards, O'Neill, and Poon[28]). We stress that the $\phi_m^\mu(\sigma^*)$ curve may also be understood as a volume-fraction-dependent yield stress, $\sigma_y^*(\phi)$, identifying the two regions where the suspension is either jammed or flowing.

This same interpretation is implicit in the work by Singh *et al.*[33], where the viscosity law of an adhesive particle suspension is described as the superposition of a Herschel-Buckley law and the viscosity of a suspension with discontinuous shear-thickening (DST). The result is the definition of a phase space (ϕ, σ^*) where the flow area is bounded at low stresses by the yield stress and high stresses by the DST threshold. In our case, only the low-stress threshold is present, since we consider fully frictional suspensions.

An important result of our study is the impact of friction on the maximum volume fraction (or, equivalently, on the yield stress). We recall that for friction coefficients $\mu_s \geq 0.3$, ϕ_m^μ decreases from the non-adhesive value, which depends on μ_s, to a value that is independent of it at low stress. For lower friction coefficients, the decrease is weaker. This result can be related to the model proposed by Richards *et al.*[8], which defines a stress-dependent maximum volume fraction for an

adhesive particle suspension, as a weighted average between the maximum volume fraction without adhesion ($\phi_\mu = 0.53$ in their case) and a volume fraction for an adhesive particle suspension (adhesive loose packing $\phi_{alp} = 0.35$). The weighting coefficient depends on the stress and varies as the fraction of particles in adhesive contact.

In our case, we do not manage to decrease the reduced shear stress below $\approx 0.7-0.8$, and for $\mu_s > 0.3$ all the curves $\phi_m^\mu(\sigma^*)$ seem to meet in $\phi_m^\mu \approx 0.5$. For lower friction coefficients, our data is a bit too sporadic, yet it appears that the maximum volume fraction is larger, which is consistent with the literature (see Richards *et al.*[8] and references therein). Further investigation of our data and comparison with the model proposed by Richards *et al.*[8] is tempting, although not straightforward, since we cannot sufficiently decrease σ^* at moderate volume fraction for ϕ_{alp} to be reliably determined.

This latter point requires further investigation. The mechanisms leading to shear-banding are unclear. The tendency of medium volume fraction suspensions to densify at low stress suggests a connection with particle clustering. Different studies, especially concerning Brownian suspensions[3], but also cohesive granular materials[73], have shown the formation of compact aggregates of various sizes which make the concentration heterogeneous and affect the rheology of the material, and this all the more as the shear stress is low. A possible explanation of the shear-banding observed in the present study would be that such aggregates develop, whose size would grow as the stress is decreased, and that shear-banding occurs as the cluster size reaches the size of our system. We note that the good agreement between the simulations in bounded and fully periodic cases does not preclude such an explanation, since in both cases, a cut-off length exists for the cluster size. A quantitative study of such a behavior requires a reliable identification of the clusters, which is not straightforward in three-dimensional systems, and which we plan to implement in the future. In addition, such an explanation implies that the too-small size of our simulation volume is at the origin of the wall-depletion and the shear-banding that we observe. A systematic increase in the size of the domain would be interesting, albeit at a high computational cost that we may be able to bear in the future.

The idea of cluster formation is also supported by the PDF of contacting particles at medium volume fraction in the non-arrested flow regime, which shows a growing isotropy in the plane of shear as the shear stress is decreased (Fig. 24), also apparent in the distribution of adhesive forces between contacting particles (Figs. 25 and 26). Thus, the depletion area in the extensional quadrant of the ambient shear flow observed in non-adhesive suspensions is progressively filled, indicating that the particles remain attached. A more comprehensive study of the PDF would certainly be of interest in the characterization of the clusters.

It should also be noted that the present simulations are carried out at controlled apparent shear rate, which may as well play a role in the development of the instability. In more detail, as regions of smaller and larger volume fraction appear, the overall shear stress decreases, which may drive the system towards the jammed state. In order to investigate this specific point, simulations at controlled stress are required. Although our simulation code does not currently provide such a feature, we are working on it.

ACKNOWLEDGMENTS

This work was supported by the French National Agency (ANR) under the program Blanc AMARHEO (ANR-18-CE06-0009-01). This work was also supported by the French government through the France 2030 investment plan managed by the National Research Agency (ANR), as part of the Initiative of Excellence Université Côte d'Azur under reference number ANR-15-IDEX-01. The authors are grateful to the Université Côte d'Azur's Center for High-Performance Computing (OPAL infrastructure) for providing resources and support. This project was also provided with computer and storage resources by GENCI at TGCC thanks to the grant 2021-gen13083 on the supercomputer Joliot Curie's the SKL and ROME partitions.

The authors are pleased to acknowledge Stany Gallier for fruitful discussions and for providing unpublished data. They warmly thank Maeva Antoine for their technical help concerning the HPC facilities and more generally for her unwavering support.

DATA AVAILABILITY STATEMENT

The data supporting the findings of this study is available within the article and from the corresponding author upon reasonable request.

Appendix A: Material functions: raw data

In Fig. 27, the shear stress is shown as a function of the shear rate: yield stresses are quite visible for the two curves for $\mu_s = 0.5$ with the highest volume fractions ($\phi_{\text{core}} \approx 0.47$ and $\phi_{\text{core}} \approx 0.48$), for which the stress seems to level off at low shear rate. For lower values of the friction coefficient the results are more difficult to interpret because, as already

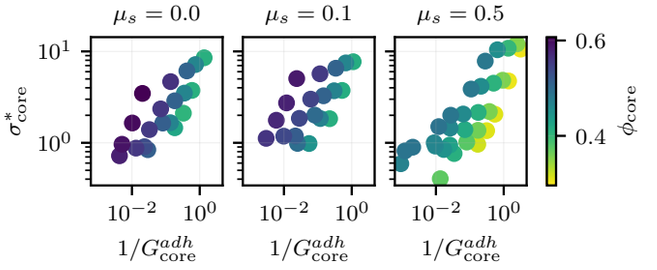

FIG. 27. Reduced shear stress as a function of the reduced shear rate, for the three friction coefficients. The color of the points is related to the core volume fraction (the higher ϕ_{core}, the darker the color).

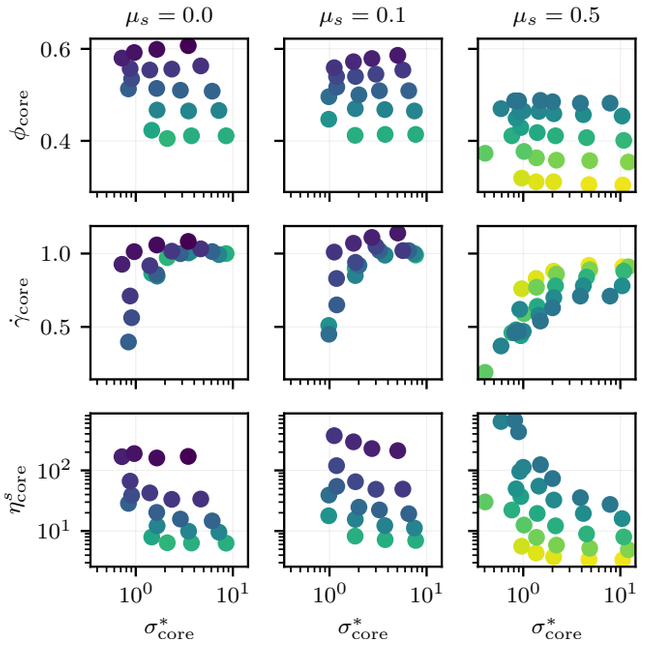

FIG. 28. Core material functions for (left column) $\mu_s = 0$, (central column) $\mu_s = 0.1$, and (right column) $\mu_s = 0.5$: (top row) core volume fraction, (central row) core shear rate, and (bottom row) core relative viscosity, as functions of the reduced shear stress. The color of the points is related to the core volume fraction (the darker the color, the higher ϕ_{core}).

pointed out, the core volume fraction is not constant when varying the shear stress.

As shown in Fig. 28 [top], and as we already explained for $\mu_s = 0.5$, the core volume fraction ϕ_{core} is rarely constant when decreasing the shear stress. For $\mu_s = 0$ and $\mu_s = 0.1$, we even tried to decrease ϕ_0 when increasing G_0^{adh} (recall Table I) aiming at obtaining a more or less constant ϕ_{core}: however, we notice that we still got an increase of ϕ_{core} for low volume fractions (indicating that a stronger decrease is needed, or that we are approaching the shear-banding regime), and for the high ones we got a decrease of ϕ_{core} (indicating that a weaker or no preventive decrease should be needed). Also, the relative viscosity η^s_{core} increases when decreasing the shear stress and approaching $\sigma^*_c \sim 1$: the effect is more pronounced for $\mu_s = 0.5$, and less visible for the other friction coefficients, due to the decrease of ϕ_{core}, which shades the increase of the viscosity.

Appendix B: JKR contact theory

In Section II D, we presented the contact model employed in the current work. Let us now recall the main features of the contact theory for the normal force developed by Johnson, Kendall, and Roberts [54] and let us see the differences with the model chosen here. The contact of two perfectly smooth spheres is considered (Fig. 29), R_1 (resp. R_2) in radius. The Young modulus and Poisson coefficient of the corresponding materials are denoted by E_1 and ν_1 (resp. E_2 and ν_2). The contact region is a disk with radius a and the contact interference, i.e., the approach of the sphere centers from the contact point, is denoted by δ. The contact region generates the surface energy:

$$U_S = -2\gamma\pi a^2 \,. \tag{B1}$$

and the total contact load is denoted by P. According to Johnson, Kendall, and Roberts [54], P, δ and a are related by the following equations:

$$P(a) = \frac{4E^* a^3}{3R} - \sqrt{16\pi\gamma E^* a^3} \,. \tag{B2}$$

$$\delta(a) = \frac{a^2}{R} - \left(\frac{\pi\gamma a}{E^*}\right)^{1/2} \,. \tag{B3}$$

Eqs. (B2) and (B3) define the JKR adhesive contact law. Before explaining these equations in some detail, they are made dimensionless. The minimum net contact force corresponds to contact radius a_c:

$$a_c = \left(\frac{9}{4}\frac{\pi R^2\gamma}{E^*}\right)^{1/3} \,. \tag{B4}$$

We can define the associated critical load as:

$$P_c = P(a_c) = -3\pi R\gamma \,. \tag{B5}$$

Let us now introduce the following dimensionless expressions, represented in Fig. 30:

$$\begin{aligned} \frac{P}{P_c} &= \mathrm{f}\left(\frac{a}{a_c}\right) = \left(\frac{a}{a_c}\right)^3 - 2\left(\frac{a}{a_c}\right)^{3/2} \,, \\ \frac{R\delta}{a_c^2} &= \mathrm{f}\left(\frac{a}{a_c}\right) = \left(\frac{a}{a_c}\right)^2 - \frac{4}{3}\left(\frac{a}{a_c}\right)^{1/2} \,. \end{aligned} \tag{B6}$$

We note that in both equations in Eq. (B6), the first term of the RHS corresponds to Hertz law without adhesion. When the two bodies are loaded by a compressive force, the adhesive forces pull the surfaces into contact over an area that exceeds the one given by Hertz theory (see Fig. 30 [a]); zero load

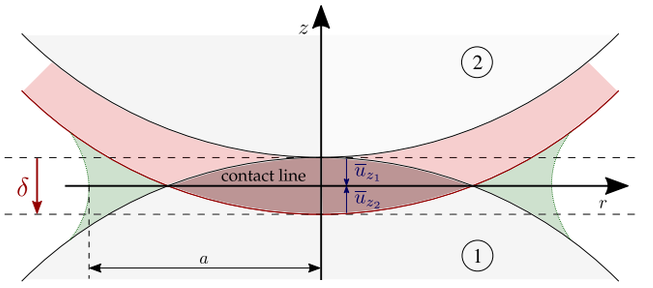

FIG. 29. Two elastic spheres at contact: from an initial position at which $\delta = 0$, sphere 2 moves towards sphere 1 with a displacement $\delta > 0$. $\overline{u}_{z_1}$ and $\overline{u}_{z_2}$ are the vertical displacement of the surface of each body due to contact pressure.

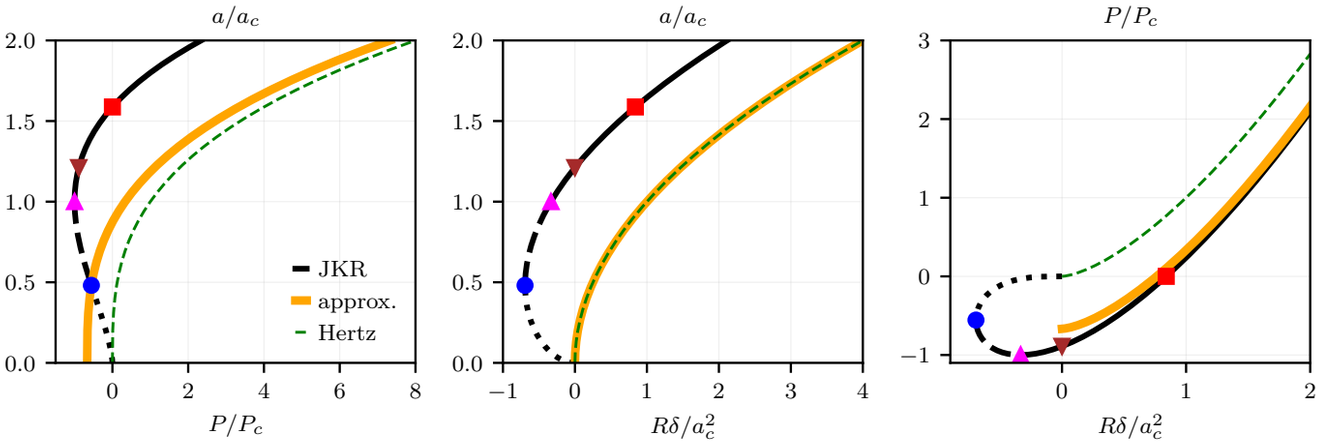

FIG. 30. (left) normalized contact area radius a/a_c versus normalized load P/P_c, (center) normalized contact area radius a/a_c versus normalized compression $\delta/\left(a_c^2/R\right)$, and (right) normalized load P/P_c versus the normalized compression $\delta/\left(a_c^2/R\right)$. Black line: JKR model. Black dashed line: unstable part of JKR curve. Green ashed line: non-adhesive Hertz model. Orange thick line: approximate model. The symbols correspond to specific steps according to JKR model(■) point at which the load is zero; (▼) point at which the compression (and thus the separation distance) is zero; (▲) point of maximum tensile load, i.e., $a = a_c$ and $P = -P_c$. It is the point after which the situation becomes unstable upon separating the particles at controlled load, leading to contact loss; (●) point of minimum compression at which the situation becomes unstable and the surfaces separate.

leaves the surfaces adhering together with a finite area and a positive compression δ; a tensile (negative) load causes the contact area to shrink further; beyond the (▲) point ($P = -P_c$, and $a = a_c$), the situation becomes unstable and they separate. The latter is true only when the load is imposed; if we impose the separation distance, this part of the curve is stable and the point (●) can be reached without separation, meaning that the (negative) compression δ can be further decreased (Fig. 30 [center]).

Before proceeding, it should be noted that Johnson, Kendall, and Roberts [54] also propose in their paper an approximate theory in which the Hertz relation between the contact area and the compression holds $a^2 = R\delta$, and surface energy is added to Hertz elastic energy:

$$U_T^{app} = \frac{8}{15}E^*\left(R\delta^5\right)^{1/2} - 2\gamma\pi R\delta \ . \tag{B7}$$

In this case, the normal load writes:

$$P^{approx} = \frac{\mathrm{d}U_T^{app}}{\mathrm{d}\delta} = \frac{4}{3}E^*\left(R\delta^3\right)^{1/2} - 2\gamma\pi R = F^{el} - F^{adh} \ , \tag{B8}$$

with $F^{adh} = 2P_c/3$, leading to:

$$\begin{aligned} \left(\frac{P}{P_c}\right)^{approx} &= \left(\frac{a}{a_c}\right)^3 - \frac{2}{3} \ , \\ \left(\frac{R\delta}{a_c^2}\right)^{approx} &= \left(\frac{a}{a_c}\right)^2 \ , \end{aligned} \tag{B9}$$

We note that the relation between the load P and the compression δ in Eq. (B8) is formally identical to the modeling that is used in the present work (Eq. (14)). This approximate approach is compared with the complete JKR theory in Fig. 30, where the corresponding relations in the frame of non-adhesive Hertz contact are displayed as well for the sake of completeness.

In Fig. 30 [left] and [center] the reduced contact area radius is represented as a function of both the reduced load and the reduced compression, while in Fig. 30 [right] the reduced normal load is represented as a function of the reduced compression. According to the JKR theory, the contact area decreases with the compression δ until separation (point (●), $\delta_{min} < 0$). Regarding the load, after a_c is reached (▲) the load slightly increases again. Thus, for both the JKR model and the approximate theory a tensile (i.e., adhesive) force can exist for positive compression (please note the zero compression point ▼ at $\delta = 0$). Moreover, at zero load there exists a positive compression (point ■), at which the associated elastic force counterbalances the attractive one. Additionally, the area of contact is an increasing function of the load for $P > -P_c$. However, the approximate theory does not allow contact for $\delta < 0$, and the area of contact is zero at maximum traction ($\delta = 0$), which is not true for the JKR model. Indeed, in the frame of the JKR model, contact is maintained for negative displacement. We suppose that the slight difference in the force at small positive values of δ does not have a qualitative effect on suspensions; anyway, this difference quickly vanishes for higher values of δ. The latter discrepancy ($a = 0$ for $P = -F^{adh}$) is important for frictional contact, as explained in the following.

In Fig. 31 the maximum value of the tangential force against the normal load is shown. The most natural way of including friction in the JKR model would be to assume that the largest friction force that the contact can bear before sliding is proportional to the contact area. Considering the curve for $P \geq -P_c$ and $a \geq a_c$ (otherwise the situation may be unstable): $\max\left(F_t\right)$ is never zero, as $a_c \neq 0$, meaning that friction is maintained at particle detachment point; the dependence of the normal force on the tangential one in such a frictional JKR

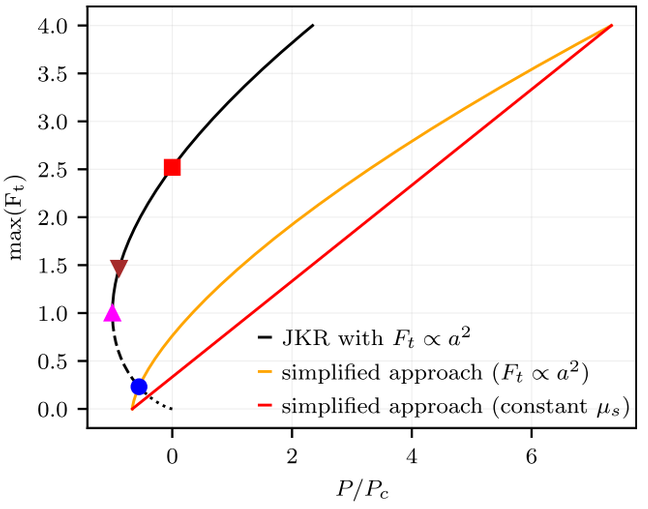

FIG. 31. Qualitative maximum value of the frictional force as a function of the normalized normal load: comparison between a frictional JKR model, a simplified approach with a variable friction coefficient, and a simplified approach with constant friction coefficient (employed in the current work). The evidenced points are the same as in Fig. 30. We recall that below point (▲) the situation is unstable.

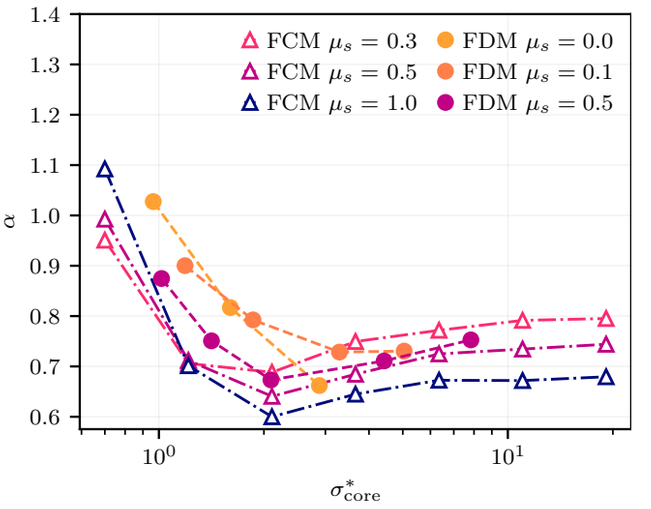

FIG. 32. Evolution of the free fitting parameter α as a function of the reduced shear stress σ^* for different friction coefficients μ_s, obtained when fitting the simulation data with the Maron-Pierce correlation law (Eq. (23)).

model is not linear, as displayed in Fig. 31.

If the same relation $F_t \propto a^2$ is assumed in the simplified approach, the relation between F_t and P is not linear either, but in that case, it vanishes for the largest traction. The influence of the precise relation between friction force and load in the context of particulate suspension surely deserves a specific study. We note that in the field of non-adhesive particle suspensions, this issue has been partly addressed. In more detail, in most of the computational work, a constant friction coefficient has been used ($F_t \propto P$), yield stress rate-independent rheology. However, if a mono-contact is assumed, the friction coefficient decreases with load, and shear-thinning behavior is observed[6]. This question is out of the scope of the present study since we do not want to precisely conclude on the nature of adhesive contact in a specific suspension, but rather to evaluate the influence of coupled friction and adhesion in the frame of a simple contact model. As a consequence, we choose a simple constant friction coefficient, using the following relation between F_t and P:

$$F_t = \mu_s \left(P + \frac{2}{3} P_c \right) . \tag{B10}$$

Such a relation is qualitatively displayed in Fig. 31.

Appendix C: Maron-Pierce fitting: $\alpha(\sigma^*)$

Here, we show the evolution of the free fitting parameter α with the reduced shear stress σ^* for different friction coefficients μ_s, obtained when fitting the Maron-Pierce correlation law (Eq. (23))to the FDM and the FCM viscosities as a function of volume fraction. In particular, the variation of $\alpha(\sigma^*)$ between 0.65 and 1 causes a residual dispersion of the viscosity when plotted against the reduced volume fraction $\phi/\phi_m^\mu(\sigma^*)$ (Fig. 14).

[1] R. G. Larson, *The Structure and Rheology of Complex Fluids* (Oxford University Press, 1999).
[2] J. Mewis and N. J. Wagner, *Colloidal Suspension Rheology*, 1st ed. (Cambridge University Press, 2011).
[3] N. Koumakis, E. Moghimi, R. Besseling, W. C. K. Poon, J. F. Brady, and G. Petekidis, "Tuning colloidal gels by shear," Soft Matter **11**, 4640–4648 (2015).
[4] R. Hoffman, "Discontinuous and dilatant viscosity behavior in concentrated suspensions. i. observation of a flow instability," Transactions of the Society of Rheology **16**, 155–173 (1972).
[5] F. Gadala-Maria and A. Acrivos, "Shear-Induced Structure in a Concentrated Suspension of Solid Spheres," Journal of Rheology **24**, 799–814 (1980).
[6] L. Lobry, E. Lemaire, F. Blanc, S. Gallier, and F. Peters, "Shear thinning in non-Brownian suspensions explained by variable friction between particles," Journal of Fluid Mechanics **860**, 682–710 (2019).
[7] J. Z. Q. Zhou, R. H. T. Uhlherr, and F. T. Luo, "Yield stress and maximum packing fraction of concentrated suspensions," Rheologica Acta **34**, 544–561 (1995).
[8] J. Richards, B. Guy, E. Blanco, M. Hermes, G. Poy, and W. Poon, "The role of friction in the yielding of adhesive non-brownian suspensions," Journal of Rheology **64**, 405–412 (2020).
[9] D. Gilbert, R. Valette, and E. Lemaire, "Impact of particle stiffness on shear-thinning of non-Brownian suspensions," Journal of Rheology **66**, 161–176 (2022).
[10] E. Lemaire, F. Blanc, C. Claudet, S. Gallier, L. Lobry, and F. Peters, "Rheology of non-Brownian suspensions: A rough contact story," Rheologica Acta (2023), 10.1007/s00397-023-01394-z.
[11] R. Seto, R. Mari, J. F. Morris, and M. M. Denn, "Discontinuous Shear Thickening of Frictional Hard-Sphere Suspensions," Physical Review Letters **111**, 218301 (2013).
[12] S. Gallier, E. Lemaire, L. Lobry, and F. Peters, "A fictitious domain approach for the simulation of dense suspensions," Journal of Computational Physics **256**, 367–387 (2014).
[13] R. Mari, R. Seto, J. F. Morris, and M. M. Denn, "Shear thickening, frictionless and frictional rheologies in non-Brownian suspensions," Journal of Rheology **58**, 1693–1724 (2014).

[14]J. Comtet, G. Chatté, A. Nigues, L. Bocquet, A. Siria, and A. Colin, "Pairwise frictional profile between particles determines discontinuous shear thickening transition in non-colloidal suspensions," Nature communications **8**, 15633 (2017).
[15]J. F. Morris, "Lubricated-to-frictional shear thickening scenario in dense suspensions," Physical Review Fluids **3**, 110508 (2018).
[16]M. Arshad, A. Maali, C. Claudet, L. Lobry, F. Peters, and E. Lemaire, "An experimental study on the role of inter-particle friction in the shear-thinning behavior of non-Brownian suspensions," Soft Matter **17**, 6088–6097 (2021).
[17]A. V. N. Le, A. Izzet, G. Ovarlez, and A. Colin, "Solvents govern rheology and jamming of polymeric bead suspensions," Journal of Colloid and Interface Science **629**, 438–450 (2023).
[18]M. Kawaguchi, A. Mizutani, Y. Matsushita, and T. Kato, "Influence of nonadsorbed polymer chains on rheology of silica suspensions," Langmuir **13**, 6339–6341 (1997).
[19]E. Koos and N. Willenbacher, "Capillary forces in suspension rheology," Science **331**, 897–900 (2011).
[20]C. S. Hodges, J. A. Cleaver, M. Ghadiri, R. Jones, and H. M. Pollock, "Forces between polystyrene particles in water using the afm: Pull-off force vs particle size," Langmuir **18**, 5741–5748 (2002).
[21]N. M. James, C.-P. Hsu, N. D. Spencer, H. M. Jaeger, and L. Isa, "Tuning interparticle hydrogen bonding in shear-jamming suspensions: Kinetic effects and consequences for tribology and rheology," The journal of physical chemistry letters **10**, 1663–1668 (2019).
[22]M. Doi and D. Chen, "Simulation of aggregating colloids in shear flow," The Journal of Chemical Physics **90**, 5271–5279 (1989).
[23]J. J. J. Gillissen, A. Papadopoulou, S. Balabani, M. K. Tiwari, and H. J. Wilson, "Suspension rheology of adhesive particles at high shear-rates," Physical Review Fluids **5**, 053302 (2020).
[24]A. Papadopoulou, J. J. Gillissen, H. J. Wilson, M. K. Tiwari, and S. Balabani, "On the shear thinning of non-Brownian suspensions: Friction or adhesion?" Journal of Non-Newtonian Fluid Mechanics **281**, 104298 (2020).
[25]H. A. Barnes, "The yield stress — a review or 'Panta rei' — Everything flows?" Journal of Non-Newtonian Fluid Mechanics **81**, 133–178 (1999).
[26]M. Wyart and M. Cates, "Discontinuous shear thickening without inertia in dense non-Brownian suspensions," Physical Review Letters **112**, 098302 (2014), arxiv:1311.4099 [cond-mat].
[27]B. M. Guy, J. A. Richards, D. J. M. Hodgson, E. Blanco, and W. C. K. Poon, "Constraint-Based Approach to Granular Dispersion Rheology," Physical Review Letters **121**, 128001 (2018).
[28]J. A. Richards, R. E. O'Neill, and W. C. Poon, "Turning a yield-stress calcite suspension into a shear-thickening one by tuning inter-particle friction," Rheologica Acta **60**, 97–106 (2021).
[29]C.-P. Hsu, J. Mandal, S. N. Ramakrishna, N. D. Spencer, and L. Isa, "Exploring the roles of roughness, friction and adhesion in discontinuous shear thickening by means of thermo-responsive particles," Nature Communications **12**, 1477 (2021).
[30]S. Pednekar, J. Chun, and J. F. Morris, "Simulation of shear thickening in attractive colloidal suspensions," Soft Matter **13**, 1773–1779 (2017).
[31]B. M. Guy, M. Hermes, and W. C. K. Poon, "Towards a Unified Description of the Rheology of Hard-Particle Suspensions," Physical Review Letters **115**, 088304 (2015).
[32]E. Brown, N. A. Forman, C. S. Orellana, H. Zhang, B. W. Maynor, D. E. Betts, J. M. DeSimone, and H. M. Jaeger, "Generality of shear thickening in dense suspensions," Nature materials **9**, 220–224 (2010).
[33]A. Singh, S. Pednekar, J. Chun, M. M. Denn, and J. F. Morris, "From yielding to shear jamming in a cohesive frictional suspension," Physical Review Letters **122**, 098004 (2019), arxiv:1809.06020.
[34]R. Yang, R. Zou, and A. Yu, "Computer simulation of the packing of fine particles," Physical review E **62**, 3900 (2000).
[35]W. Liu, Y. Jin, S. Chen, H. A. Makse, and S. Li, "Equation of state for random sphere packings with arbitrary adhesion and friction," Soft Matter **13**, 421–427 (2017).
[36]Z. Ge, R. Martone, L. Brandt, and M. Minale, "Irreversibility and rate dependence in sheared adhesive suspensions," Physical Review Fluids **6**, L101301 (2021).
[37]M. Orsi, L. Lobry, and F. Peters, "Frame-invariant sub-grid corrections to the Fictitious Domain Method for the simulation of particulate suspensions in nonlinear flows using OpenFOAM," Journal of Computational Physics **474**, 111823 (2023).
[38]K. Yeo and M. R. Maxey, "Dynamics of concentrated suspensions of non-colloidal particles in Couette flow," Journal of Fluid Mechanics **649**, 205–231 (2010).
[39]M. Orsi, *Simulation of concentrated non-Brownian frictional and adhesive suspensions in linear and nonlinear flows*, PhD dissertation, Université Côte d'Azur, CNRS, Institut de Physique de Nice (2022).
[40]G. K. Batchelor, "The stress system in a suspension of force-free particles," Journal of Fluid Mechanics **41**, 545–570 (1970).
[41]D. Lhuillier, "Migration of rigid particles in non-Brownian viscous suspensions," Physics of Fluids **21**, 023302 (2009).
[42]P. R. Nott, E. Guazzelli, and O. Pouliquen, "The suspension balance model revisited," Physics of Fluids **23**, 043304 (2011).
[43]D. J. Jeffrey, J. F. Morris, and J. F. Brady, "The pressure moments for two rigid spheres in low-Reynolds-number flow," Physics of Fluids A: Fluid Dynamics **5**, 2317–2325 (1993).
[44]K. Yeo and M. R. Maxey, "Simulation of concentrated suspensions using the force-coupling method," Journal of Computational Physics **229**, 2401–2421 (2010).
[45]F. Peters, G. Ghigliotti, S. Gallier, F. Blanc, E. Lemaire, and L. Lobry, "Rheology of non-Brownian suspensions of rough frictional particles under shear reversal: A numerical study," Journal of Rheology **60**, 715–732 (2016).
[46]M. R. Maxey, "Simulation Methods for Particulate Flows and Concentrated Suspensions," Annual Review of Fluid Mechanics **49**, 171–193 (2017).
[47]K. Yeo, *Some Aspects of Suspension Flows: Stokes to Turbulent Flows*, Ph.D. thesis, Brown University (2011).
[48]S. Plimpton, "Fast parallel algorithms for short-range molecular dynamics," Journal of Computational Physics **117**, 1–19 (1995).
[49]M. Orsi, L. Lobry, E. Lemaire, and F. Peters, "Mass and momentum balance during particle migration in the pressure-driven flow of frictional non-brownian suspensions," Journal of Fluid Mechanics **998**, A16 (2024).
[50]A. A. Howard, M. R. Maxey, and S. Gallier, "Bidisperse supension balance model," Physical Review Fluids **7**, 124301 (2022).
[51]K. L. Johnson, *Contact Mechanics* (Cambridge University Press, 1985).
[52]A. Kumar, T. Staedler, and X. Jiang, "Role of relative size of asperities and adhering particles on the adhesion force," Journal of colloid and interface science **409**, 211–218 (2013).
[53]Y. Zou, S. Jayasuriya, C. W. Manke, and G. Mao, "Influence of nanoscale surface roughness on colloidal force measurements," Langmuir **31**, 10341–10350 (2015).
[54]K. L. Johnson, K. Kendall, and A. D. Roberts, "Surface energy and the contact of elastic solids," Proc. R. Soc. Lond. A. **324**, 301–313 (1971).
[55]S. Gallier, E. Lemaire, F. Peters, and L. Lobry, "Rheology of sheared suspensions of rough frictional particles," Journal of Fluid Mechanics **757**, 514–549 (2014).
[56]B. Derjaguin, "Molekulartheorie der äußeren Reibung," Zeitschrift für Physik **88**, 661–675 (1934).
[57]F. Blanc, F. Peters, and E. Lemaire, "Experimental Signature of the Pair Trajectories of Rough Spheres in the Shear-Induced Microstructure in Non-colloidal Suspensions," Physical Review Letters **107**, 208302 (2011).
[58]P. Pham, B. Metzger, and J. E. Butler, "Particle dispersion in sheared suspensions: Crucial role of solid-solid contacts," Physics of Fluids **27**, 051701 (2015).
[59]R. V. More and A. M. Ardekani, "Effect of roughness on the rheology of concentrated non-brownian suspensions: A numerical study," Journal of Rheology **64**, 67–80 (2020).
[60]P. Cundall and O. Strack, "Discussion: A discrete numerical model for granular assemblies," Géotechnique **30**, 331–336 (1980).
[61]F. Blanc, F. Peters, and E. Lemaire, "Local transient rheological behavior of concentrated suspensions," Journal of Rheology **55**, 835–854 (2011).
[62]R. I. Tanner and S. Dai, "Particle roughness and rheology in noncolloidal suspensions," Journal of Rheology **60**, 809–818 (2016).
[63]A. Singh, R. Mari, M. M. Denn, and J. F. Morris, "A constitutive model for simple shear of dense frictional suspensions," Journal of Rheology **62**, 457–468 (2018).

[64]J. F. Morris and F. Boulay, "Curvilinear flows of noncolloidal suspensions: The role of normal stresses," Journal of Rheology **43**, 1213–1237 (1999).
[65]A. A. Howard, J. Dong, R. Patel, M. D'Elia, M. R. Maxey, and P. Stinis, "Machine learning methods for particle stress development in suspension poiseuille flows," Rheologica Acta **62**, 507–534 (2023).
[66]W. Peerbooms, T. Nadorp, A. van der Heijden, and W.-P. Breugem, "Interparticle friction in sheared dense suspensions: Comparison of the viscous and frictional rheology descriptions," Journal of Rheology **68**, 263–283 (2024).
[67]A. Badia, Y. D'Angelo, F. Peters, and L. Lobry, "Frame-invariant modeling for non-Brownian suspension flows," Journal of Non-Newtonian Fluid Mechanics **309**, 104904 (2022).
[68]S. Gallier, F. Peters, and L. Lobry, "Simulations of sheared dense noncolloidal suspensions: Evaluation of the role of long-range hydrodynamics," Physical Review Fluids **3**, 042301 (2018).
[69]P. Snabre and P. Mills, "Rheology of Weakly Flocculated Suspensions of Rigid Particles," Journal de Physique III **6**, 1811–1834 (1996).
[70]W. Chèvremont, B. Chareyre, and H. Bodiguel, "Quantitative study of the rheology of frictional suspensions: Influence of friction coefficient in a large range of viscous numbers," Physical Review Fluids **4**, 064302 (2019).
[71]F. Boyer, É. Guazzelli, and O. Pouliquen, "Unifying Suspension and Granular Rheology," Physical Review Letters **107**, 188301 (2011).
[72]F. Blanc, E. D'Ambrosio, L. Lobry, F. Peters, and E. Lemaire, "Universal scaling law in frictional non-Brownian suspensions," Physical Review Fluids **3**, 114303 (2018).
[73]P. Rognon, J.-N. Roux, M. Naaim, and F. Chevoir, "Dense flows of cohesive granular materials," (2008).
[74]S. Mandal, M. Nicolas, and O. Pouliquen, "Rheology of cohesive granular media: Shear banding, hysteresis, and nonlocal effects," Physical Review X **11**, 021017 (2021).
[75]J. F. Morris, "A review of microstructure in concentrated suspensions and its implications for rheology and bulk flow," Rheologica acta **48**, 909–923 (2009).
[76]É. Guazzelli and O. Pouliquen, "Rheology of dense granular suspensions," Journal of Fluid Mechanics **852** (2018), 10.1017/jfm.2018.548.
[77]F. Blanc, E. Lemaire, A. Meunier, and F. Peters, "Microstructure in sheared non-Brownian concentrated suspensions," Journal of Rheology **57**, 273–292 (2013).